Modeling mineral dust emissions from the Sahara desert using new surface properties and soil database

B. Laurent, B. Marticoréna, G. Bergametti, J. F. Leon, N. M Mahowald

JOURNAL OF GEOPHYSICAL RESEARCH, VOL. 113, D14218, doi:10.1029/2007JD009484, 2008

Modeling mineral dust emissions from the Sahara desert using new surface properties and soil database

B. Laurent,[1,2] B. Marticorena,[1] G. Bergametti,[1] J. F. Léon,[3] and N. M. Mahowald[4]

Received 10 October 2007; revised 24 January 2008; accepted 26 February 2008; published 30 July 2008.

[1] The present study investigates the mineral dust emissions and the occurrence of dust emission events over the Sahara desert from 1996 to 2001. Mineral dust emissions are simulated over a region extending from 16°N to 38°N and from 19°W to 40°E with a $^1/_4^\circ \times {}^1/_4^\circ$ spatial resolution. The input parameters required by the dust emission model are surface features data (aerodynamic roughness length, dry soil size distribution and texture for erodible soils), and meteorological surface data (mainly surface wind velocity and soil moisture). A map of the aerodynamic roughness lengths is established based on a composition of protrusion coefficients derived from the POLDER-1 surface products. Soil dry size distribution and texture are derived from measurements performed on soil samples from desert areas, and from a soil map derived from a geomorphologic analysis of desert landscapes. Surface re-analyzed meteorological databases (ERA-40) of the European Centre for Medium range Weather Forecasts (ECMWF) are used. The influence of soil moisture on simulated dust emissions is quantified. The main Saharan dust sources identified during the 6-year simulated period are in agreement with the previous studies based on in situ or satellite observations. The relevance of the simulated large dust sources and point sources (''hot spots'') is tested using aerosol indexes derived from satellite observations (TOMS Absorbing Aerosol Index and Infrared Dust Difference Index Meteosat). The Saharan dust emissions simulated from 1996 to 2001 range from 585 to 759 Tg a^{-1}. The simulations show marked seasonal cycles with a maximum in summer for the western Sahara and in spring for the eastern Sahara. The interannual variability of dust emissions is pronounced in the eastern part of the Sahara while the emissions from the western Sahara are more regular over the studied period. The soil moisture does not noticeably affect the Saharan dust emissions, their seasonal cycle or their interannual variability, but it can partly control and limit the dust emissions in some parts of the northern desert margin, where the precipitation rates are higher. Our simulations also tend to confirm that the Sahara is the major terrestrial source of mineral dust.

Citation: Laurent, B., B. Marticorena, G. Bergametti, J. F. Léon, and N. M. Mahowald (2008), Modeling mineral dust emissions from the Sahara desert using new surface properties and soil database, *J. Geophys. Res.*, *113*, D14218, doi:10.1029/2007JD009484.

1. Introduction

[2] Atmospheric mineral dust is mainly produced by the aeolian erosion acting in arid and semi-arid areas. Mineral aerosols have an impact on the Earth's radiative budget by absorbing and scattering incoming solar and outgoing terrestrial radiations [e.g., *Sokolik and Toon*, 1999]. As neither the sign nor the intensity of this dust radiative effect is assessed nowadays, it is one of the major uncertainties on the evaluation of climatic changes. Mineral dust is involved in heterogeneous and multiphase atmospheric chemistry, affecting photo-oxydant concentrations and the composition of precipitation [*Loÿe-Pilot et al.*, 1986; *Losno et al.*, 1991; *Bauer et al.*, 2004]. It also contributes to the biogeochemical cycles of many elements, and in particular those of nutrients like Fe and P suspected to be limiting in isolated ecosystems (e.g., open oceans, the Amazon forest) [*Bergametti et al.*, 1992; *Swap et al.*, 1992; *Jickells et al.*, 2005].

[3] The Sahara desert is generally considered as the major source of mineral dust [*Prospero et al.*, 2002; *Washington et al.*, 2003]. However, estimations of the Saharan dust emissions are generally derived from information on transported dust: atmospheric concentration, aerosol optical thickness or deposition fluxes downwind of the north African continent [*Andreae*, 1995; *Duce*, 1995; *Koren et al.*, 2006], since over the North of Africa only semiquantitative information (aerosol indexes) derived from satellite observations are available up to now. These estimations fluctuate between 130 and 1600 Tg a^{-1} [*Goudie and Middleton*, 2001;

[1]Laboratoire Interuniversitaire des Systèmes Atmosphériques, Universités Paris VII-XII, Créteil, France.
[2]Now at Leibniz-Institut für Troposphärenforschung, Leipzig, Germany.
[3]Laboratoire d'Optique Atmosphérique, Université des Sciences et Technologies Lille, Villeneuve-d'Ascq, France.
[4]Department of Earth and Atmospheric Sciences, Cornell University, New York, USA.

0148-0227/08/2007JD009484$09.00

Engelstaedter et al., 2006]. Global mineral dust emissions estimated from modeling approaches range from 1000 to 3000 Tg a^{-1} [*Duce*, 1995; *Zender et al.*, 2004; *Cakmur et al.*, 2006]. This reflects differences in the estimation methods, including differences in parameterization of the dust emission processes, in input parameters of surface properties, and also in the simulated period.

[4] In this work, we estimate the Saharan dust emission occurrences and intensities, their seasonal interannual variability, and the location of main Saharan source areas. Both the quality of the physical model used and the relevance of the new surface and soil databases developed in this work allow a deeper analysis of the mineral dust emissions. This analysis is based on simulations performed with a physically explicit dust emission scheme (without any adjustment factor) representing the present state of the art in term of dust emissions at the continental scale. Surface parameters controlling dust emissions are derived from experimental data or satellite observations, without any a priori hypothesis on the efficiency of the different surface types to produce mineral dust. The results thus illustrate how well our current knowledge (of the dust production processes and of the desert surface properties) allows to simulate the dust emissions. The validation of Saharan dust emission simulation appears as a complex issue since there are no direct quantitative measurements of the dust emissions at a continental scale. Our strategy is thus to use all available proxies of the mineral dust content over the North of Africa and in the neighboring areas to test the main trends identified in the simulation. This concerns the location of the main dust source regions and the spatial variability of the seasonal cycle.

[5] The physical dust emission model and the parameterizations of the main dust production processes used are described in section 2. The method developed to establish accurate soil and surface databases and the description of the meteorological fields used are described in section 3. The results of the simulations of Saharan dust emissions performed from 1996 to 2001 are discussed and compared to observations in section 4, and the main concluding points are gathered in a final section.

2. Dust Emission Model

[6] The physical dust emission scheme initially developed and validated by *Marticorena and Bergametti* [1995], *Marticorena et al.* [1997a, 1997b], and *Fécan et al.* [1999] is used. The input parameters required for a large scale application of this physical scheme and the way they can be retrieved are fully described by *Marticorena et al.* [1997a, 2004] and *Callot et al.* [2000]. The main steps of the dust emission processes and the dust emission model are described below.

[7] The emission of transportable soil-derived particles is a power function of the wind friction velocity (U^*) but occurs only when a threshold value in wind friction velocity (U_t^*) is reached [e.g., *Bagnold*, 1941; *Chepil*, 1951]. This erosion threshold mainly depends on the dry soil size distribution, on the roughness induced by the presence of nonerodible elements over the erodible surface, and on the soil moisture [e.g., *Gillette*, 1979].

[8] Once the erosion threshold is reached, the soil grains enter into a horizontal movement called saltation. When the saltating soil grains strikes the surface, their kinetic energy is transferred to the surface. The soil aggregates can then be disrupted if the energy provided exceeds the energy of the cohesive forces linking the dust particles into aggregates. This process, called sandblasting, is by far the main process responsible for the vertical flux of produced fine particles that can be transported over long distances [e.g., *Gillette*, 1979; *Gomes et al.*, 1990].

[9] The total amount of material mobilized by wind, or horizontal flux (G), mainly depends on the wind friction velocity and on the dry soil size distribution while the intensity of the dust flux, i.e., vertical flux (F), is mainly controlled by the ability of the soil to release fine transportable particles [*Gillette*, 1979; *Shao et al.*, 1993].

[10] The erosion threshold, the horizontal flux and dust vertical flux are parameterized in the dust emission scheme.

2.1. Erosion Thresholds

[11] It can be observed that dust emissions do not occur for any wind velocity conditions. Indeed, dust emissions only occur when the wind velocity (and thus the wind friction velocity) exceeds a certain value. This wind friction velocity value is called the threshold wind friction velocity (U_t^*). It is a key parameter in the modeling of wind erosion and dust emissions since this parameter controls both the frequency and the intensity of dust emissions. The dust emission model is first based on a parameterization of U_t^* as a function of (1) the size of the in-place erodible aggregates (D_p), (2) the aerodynamic roughness length of the overall surface (Z_0), and (3) the aerodynamic roughness length of the erodible part of the surface (z_{0s}).

[12] Experimental data from *Bagnold* [1941] and *Chepil* [1951] indicated that, for large grains, U_t^* increases when the grain size increases (due to the gravity forces). However, they also revealed an increase of U_t^* when the grain size decreases for the smallest particles (mainly due to the interparticle cohesive forces reinforcing the links between grains) [e.g., *Iversen and White*, 1982]. These two effects lead to an optimum grain size ($\sim$80 μm) for which the threshold friction velocity is the lowest. The soil grain size dependence of the erosion threshold is the adaptation proposed by *Marticorena and Bergametti* [1995] of the parameterization developed by *Iversen and White* [1982]. However, natural soils are generally composed of grains with different sizes and thus different threshold wind friction velocities. Consequently, the in situ dry soil size distribution has to be properly described (see section 3).

[13] Nonerodible elements present on the surface of arid and semiarid regions consume a part of the wind momentum that will then not be available to initiate particle motion. This leads to a global decrease of the wind shear stress acting on the erodible surface and to an apparent increase of U_t^*. A physical scheme describing the drag partition between the roughness elements (characterized by Z_0) and the erodible surface (characterized by z_{0s}) is necessary to parameterize U_t^* in ''rough'' situations which are most frequently encountered in arid and semiarid areas.

[14] In the dust emission model, the influence of the decrease in the wind shear stress due to the presence of

nonerodible elements on the surface is accounted for using the drag partition scheme developed by *Marticorena and Bergametti* [1995]:

$$U_t^*(D_p, Z_0, z_{0s}) = \frac{U_t^*(D_p)}{f_{eff}(Z_0, z_{0s})} \quad (1)$$

$$\text{with } f_{eff}(Z_0, z_{0s}) = 1 - \left(\ln\left(\frac{Z_0}{z_{0s}}\right) \Big/ \left(0.35\left(\frac{10}{z_{0s}}\right)^{0.8}\right)\right) \quad (2)$$

D_p, Z_0 and z_{0s} having units of centimeters.

[15] It has been shown [*Marticorena and Bergametti*, 1995; *Marticorena et al.*, 1997b] that this parameterization reproduces the U_t^* measured over various natural surfaces corresponding to a large range of Z_0 [*Gillette*, 1981; *Nickling and Gillies*, 1989].

[16] Another factor affecting U_t^* is the soil moisture. The soil water reinforces the cohesive forces between the soil grains and thus increases the erosion thresholds. However, soil water retention consists of molecular adsorption on the soil grains surface and capillary forces between the grains [*McKenna-Neuman and Nickling*, 1989]. Interparticle capillary forces are the main factor responsible for the increase of the wind erosion threshold observed when the soil moisture increases. Below a soil moisture content close to the maximum amount of adsorbed water (w') these capillary forces are insufficient to significantly increase the erosion threshold. Since w' depends on the soil texture, the increase in erosion threshold is different for the same soil water content depending on the soil type.

[17] A parameterization of the influence of the soil moisture on the erosion threshold was proposed by *Fécan et al.* [1999]. It allows the computation of the increase of the erosion threshold in wet conditions (U_{tw}^*) by reference to dry conditions (U_{td}^*) as a function of the soil moisture (w) and the residual soil moisture (w') (equations (3), (4), and (5)):

$$\text{for } w < w': \quad \frac{U_{tw}^*}{U_{td}^*} = 1 \quad (3)$$

$$\text{for } w > w': \quad \frac{U_{tw}^*}{U_{td}^*} = \left[1 + 1.21(w - w')^{0.68}\right]^{0.5} \quad (4)$$

with w' defined as a function of the soil clay content:

$$w' = 0.0014(\%clay)^2 + 0.17(\%clay) \quad (5)$$

w and w' having units of % (mass of water/mass of dry soil).

2.2. Erosion and Dust Fluxes

2.2.1. Horizontal Flux

[18] Many works, both theoretical and experimental [*Bagnold*, 1941; *White*, 1979; *Gillette*, 1974, 1979; *Gillette and Stockton*, 1989; *Sörensen*, 1985; *Leys and Raupach*, 1991; *Shao et al.*, 1993] showed that the horizontal flux (G) is proportional to a third power of the wind friction velocity. Using a trench on a beach, *Greeley et al.* [1996] performed horizontal flux measurements with a high confidence level (5% in mass) allowing the evaluation of the various equations proposed to retrieve G. These authors found that the model of *Bagnold* [1941] and the formulation of *White* [1979] most closely agree with the experimental data. However, since only White's equation includes a threshold term and is supported by a dimensional analysis, we can consider this one as the best available formulation for G.

[19] Including the size dependent expression of U_t^* in the *White*'s [1979] formulation provides a size-dependent equation of G. This equation allows the computation of the amount of material mobilized by wind and its size-distribution as a function of the wind friction velocity:

$$G = E\frac{\rho_a}{g}U^{*3}\int_{D_p}\left(1 + \frac{U_t^*(D_p, Z_0, z_0)}{U^*}\right) \cdot \left(1 - \frac{U_t^*(D_p, Z_0, z_0)^2}{U^{*2}}\right) dS_{rel}(D_p)\, dD_p \quad (6)$$

where E is the fraction of erodible to total surface, $dS_{rel}(D_p)$ is the relative surface covered by the particles of diameter D_p.

[20] This size-dependent representation of G provides a satisfactory reproduction of the total mass and size distribution of the horizontal fluxes measured in wind tunnels for different soil substrates and wind friction velocities by *Williams* [1964] or *Sörensen* [1985]. However, it must be noted that such a parameterization does not correctly reproduce the horizontal flux for supply limited surfaces such as crusted soils [*Lopez*, 1998].

2.2.2. Dust Vertical Flux

[21] Only physically explicit sandblasting models allow simulations of the mass and of the size-distribution of the emitted dust. The dust production corresponds to the rupturing of the interparticle bonds linking dust particles to each other or to the surface. When the saltating grains strike the surface, their kinetic energy is used to disintegrate the aggregates and to produce fine dust particles. Models were elaborated to simulate the sandblasting process [*Alfaro et al.*, 1997, 1998; *Lu and Shao*, 1999; *Alfaro and Gomes*, 2001; *Shao*, 2001].

[22] The model proposed by *Alfaro et al.* [1997, 1998] is based on the existence of different binding energies depending on the size of the emitted dust particles. These binding energies correspond to different thresholds of disruption of the aggregates. Dust of a given size is produced only when the kinetic energy of the saltating soil particles exceeds the corresponding threshold. This implies that the dust size distribution varies as a function of the size of the saltating particles and of their velocity, in agreement with wind tunnel observations [*Alfaro and Gomes*, 2001].

[23] In contrast to energy-based models, *Lu and Shao* [1999] estimated dust production as a function of the volume of soil removed by the saltating grains impacting at the surface. The saltation bombardment was considered as the main mechanism for dust production through the excavation of craters in the surface. The total volume of the soil material ejected into the air was assumed to be equal to the volume of the crater created by the saltating grains. *Shao* [2001] provided a more elaborated version of this model,

including the saltation bombardment but also the aerodynamic entrainment and the aggregate disintegration.

[24] The application of the two sandblasting models developed by *Alfaro and Gomes* [2001] and *Lu and Shao* [1999] for large scale modeling of dust emissions is extremely difficult due to the fact the required input data cannot be determined with a sufficient confidence level at such a scale. For example, the binding energies in the model of *Alfaro and Gomes* [2001] are not directly measured but indirectly determined to fit the size distributions of dust particles measured for different soils and different friction velocities (i.e., for different kinetic energies of the saltating grains). As long as these binding energies will not be directly measured, they will remain highly uncertain and will require an adjustment to fit available experimental data sets [*Gomes et al.*, 2003]. The problem is similar with the saltation bombardment model. Typically, one of the main input parameters is the soil plastic pressure, a parameter that cannot be simply measured. However, *Alfaro et al.* [2004] and *Shao* [2004] recently provided new tests of these models, and their applicability at large scale could be considered in future studies.

[25] In this study, the empirical parameterization of the sandblasting efficiency proposed by *Marticorena and Bergametti* [1995] is used. On the basis of the coupled measurements of horizontal fluxes (G) and vertical fluxes of dust particles with a diameter < 20 μm (F) by *Gillette* [1979], these authors established an empirical relationship linking the ratio of the dust flux to the horizontal flux (i.e., the sandblasting efficiency α) to the soil clay content:

$$\alpha = \frac{F}{G} = 10^{\left(0.134\left(\%_{clay}\right)-6\right)} \tag{7}$$

[26] This parameterization allows the estimation of the mass of the emitted dust but not the dust size distribution. Since it was successfully used for large scale applications [*Marticorena and Bergametti*, 1996; *Marticorena et al.*, 1997a; *Laurent et al.*, 2006], we decide to use this parameterization to compute the mass of the emitted dust and to investigate the dust emission occurrences and intensities over the North of Africa.

[27] To summarize, the model used in this study allows computing the dust flux produced by erodible loose surfaces, provided the required surface and meteorological input parameters have been specifically determined. The parameterizations of the physical process we choose to use here are commonly used to model mineral dust for large scale applications. To optimize their relevance and thus to estimate more accurately the Saharan mineral dust emissions, a new surface and soil database is developed.

3. Input Parameters

3.1. Surface Parameters

[28] Input parameters characterizing both the roughness elements and the dry soil size distribution available on the soil surface layer are required: the aerodynamic roughness length induced by the erodible surface (surface in ''smooth'' conditions, z_{0s}) and by the nonerodible obstacles (Z_0); the dry size distribution of the soil micropeds available for wind erosion; and the soil clay content which is used as an indicator of the capability of the soil to release fine particles.

3.1.1. Aerodynamic Roughness Length (Z_0)

[29] The aeolian roughness length is the most critical parameter for the estimation of the threshold wind friction velocity in the model used in this study. Since it cannot be experimentally determined over large desert surfaces such as the Sahara, it has to be estimated from other proxies.

[30] A first method to estimate the aeolian roughness length was developed for the Sahara desert by *Marticorena et al.* [1997a] and *Callot et al.* [2000]. This method, based on a geomorphologic approach, led to quite satisfying results since simulations of dust emissions using these roughness lengths compared well with satellite observations [*Marticorena et al.*, 1997a]. To be relevant, this approach requires sufficient documentations in terms of amount and confidence level and field observations that cannot be achieved in many desert areas.

[31] An alternative approach is to examine how satellite observations could provide a global mapping of the aeolian roughness lengths. *Greeley et al.* [1997] used the radar backscatter signal to retrieve the roughness heights over selected desert targets. Following this pioneer work, *Marticorena et al.* [2004] investigated the possibility to retrieve the surface roughness length of arid areas using the surface bidirectional reflectance products derived from passive multidirectional measurements in the solar spectrum of the POLarization and Directionality of the Earth Reflectance (POLDER-1) space-borne sensor. An empirical relationship between the aerodynamic roughness height and a Protrusion Coefficient (PC) derived from the POLDER-1 bidirectional reflectance distribution function (BRDF) in the visible range was established. In order to obtain a PC map as complete as possible, data sets for several months and two wavelengths (November 1996 to February 1997 at 670 nm and 865 nm; note that due to inaccurate calibration, the near UV wavelength 443 nm was not used) are used in the present study for the composition at the $^1/_{16}^\circ \times {}^1/_{16}^\circ$ full spatial resolution (see *Laurent et al.* [2005] for more details). To increase the confidence level of the final composition (quality and consistency), a selection of the monthly and composite data sets is performed. Following *Marticorena et al.* [2004] and *Laurent et al.* [2005], a composite map of the aerodynamic roughness length (Z_0) at the $^1/_{16}^\circ \times {}^1/_{16}^\circ$ full spatial resolution is established for the North of Africa (Figure 1).

[32] In the Sahara, the retrieved roughness lengths vary over more than three orders of magnitude, ranging from 10^{-3} cm up to $5\ 10^{-1}$ cm. Areas having homogeneous roughness lengths can be identified and associated to specific geomorphologic units.

[33] The Sahara includes numerous ergs made of fixed or mobile dunes with different shapes: the Great western Erg, the Great eastern Erg in Algeria; the Iguidi Erg and the Chech Erg in Mauritania, Mali, and south Algeria; the Bilma Erg and the Ténéré in Niger; the Mourzouk Erg in Libya; and the Libyan Desert that spreads from Libya to Egypt [*Mainguet and Chemin*, 1985]. The main ergs and the sandy areas exhibit the lowest Z_0, with median values between $2.6\ 10^{-3}$ cm and $7.5\ 10^{-3}$ cm [*Marticorena et al.*, 2004].

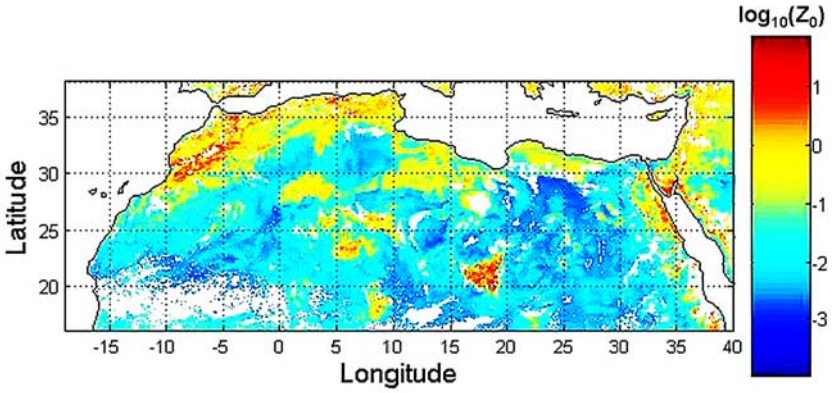

Figure 1. Map of the logarithm of the aerodynamic roughness length Z_0 with a spatial resolution of $^1/_{16}^\circ \times {}^1/_{16}^\circ$ over the North of Africa (16°N–38°N; 19°W–40°E) (Z_0 in cm).

[34] The reg surfaces are characterized by their pebble and stone covers and are a dominant landscape over the Sahara desert. The hamadas are plateaux of bare rocks, stones and pebbles. They are characterized by a higher pebble or stone cover rate than the reg surfaces located in the plains. Regs surfaces have high erosion thresholds [*Callot et al.*, 2000] and thus dust emissions are expected to be relatively infrequent on these surfaces. The regs, the hamadas and the mountains exhibit very high Z_0: typically, median values ranging from 1.1 10^{-2} cm to 3.9 10^{-2} cm are observed over the reg surfaces and values between 1.8 10^{-2} cm and 5.4 10^{-1} cm for the hamadas. The north Sahara is surrounded by the Atlas Mountains in Morocco and Algeria. Other mounts are located inside the desert: the Hoggar and Tassili N'Ajjer in south Algeria, the Aïr in Niger, the Adrar of Iforas in Mali, and the Tibesti in Chad. The rocky surfaces constituting these mountain areas are generally not erodible and are considered not to be dust sources a priori. They correspond to the highest roughness length derived from POLDER-1 observations.

[35] It must be noted that some data are missing due to the selection on the quality and the consistency of the satellite data and to persistent cloud cover, in particular in the southern part of the studied area: the southern part of Mauritania and Mali; the Bilma Erg (~18°N, 12°E); and a part of the Bodélé Depression (~17°N, 17°E). For these areas, Z_0 is estimated considering the neighboring pixel values, the Z_0 estimated from a geomorphologic analysis of north African landscapes at the 1° × 1° resolution [*Marticorena et al.*, 1997a; *Callot et al.*, 2000], and the local and regional geomorphologic and topographic context at the resolution 1/1,000,000 (*Institut Géographique National IGN, France; Military Survey, Ministry of Defense, United Kingdom; Defense Mapping Agency, Aerospace center, St Louis (USA)*).

[36] Moreover, *Marticorena et al.* [2004] and *Laurent et al.* [2005] showed that a decrease of the spatial resolution down to ¼° × ¼° did not introduce significant bias on the frequency distribution of the *PC* compared to the full resolution data set. Since this resolution is better adapted than the full one for large scale simulations [*Laurent et al.*, 2005, 2006], a complete map of the aerodynamic roughness length Z_0 with a ¼° × ¼° spatial resolution is finally established over the North of Africa.

3.1.2. Dry Soil Size Distribution

3.1.2.1. Saharan Dry Soil Size Distribution

[37] Available soil data sets [e.g., *Zobler*, 1986] generally classify soils according to the "textural triangle" defined by the three size components: sand (2000 to 80 or 63 μm), silt (80 or 63 to 4 or 2 μm) and clay (<4 or 2 μm). However, this classification is based on measurements performed by using wet sedimentation techniques (ultrasonic pretreatment, dissolution), which break the soil aggregates [*Chatenet et al.*, 1996; *Ding et al.*, 1999] and thus does not reflect the natural state of aggregation of the soil. As an example, such classification leads to relatively large amounts of loose clay particles that are generally not encountered in the natural soils as loose particles. In natural soils, these particles generally form aggregates of larger size (>50–100 μm). As a result, such a classification cannot be directly used to characterize the in situ size distributions of erodible soils. The only relevant approach is to determine the soil size distribution using soil aggregates determination by dry techniques that minimize, as much as possible, the breakage of the aggregates. Such an approach was proposed by *Chatenet et al.* [1996] for the Saharan and Sahelian soils and was also applied to Chinese soil by *Mei et al.* [2004]. Following *Chatenet et al.* [1996], we consider the soil mass distribution determined by dry sieving as lognormally distributed or as the combination of 2 or 3 different lognormal functions.

[38] For the Sahara, *Chatenet et al.* [1996] showed that the dry size distribution of any soil can be determined as a mixture of a maximum of 4 typical populations namely alumino-silicated-silt, fine sand, coarse sand and salts. The statistical parameters of the lognormal functions characterizing these 4 populations (median diameter D_{med}, and standard deviation σ) were determined from experimental data in (Table 1).

[39] To describe the north African desert soils, *Marticorena et al.* [1997a] and *Callot et al.* [2000] defined 12 soil types, each soil type being a mixture of the four populations identified by *Chatenet et al.* [1996] in various proportions (Table 1). Table 2 summarizes the statistical parameters of these 12 dry soil size distributions. Most of the soils are a

Table 1. Mineralogical Features and Lognormal Size Distribution Parameter of the Populations Identified in the Soils From Arid Areas (North of Africa), From *Chatenet et al.* [1996]

Typology	Mineralogical Feature	$D_{med,}$ μm	σ
Alumino-silicated-silt	clay mineral dominant	125	1.8
Fine sand	quartz dominant	210	1.6
Coarse sand	quartz	690	1.6
Salts	salt and clay minerals	520	1.5

combination of two populations, only two of them involve three populations.

[40] In the present study, the soil parameters initially mapped at the square degree resolution for the North of Africa by *Marticorena et al.* [1997a] and *Callot et al.* [2000] are mapped at the $1/4^\circ \times 1/4^\circ$ spatial resolution using the same geomorphologic approach. The main landscapes are localized on the $1/16^\circ \times 1/16^\circ$ full spatial resolution map of aerodynamic roughness lengths using the initial soil map using the geomorphologic information reported on topographic maps at the resolution 1/1,000,000 (*Institut Géographique National IGN, France; Military Survey, Ministry of Defense, United Kingdom; Defense Mapping Agency, Aerospace center, St Louis (USA)*).

[41] The dune shape and the dune field geomorphology are information that can be used to retrieve and estimate the size distribution of sand and then their ability to produce mineral dust [*Marticorena et al.*, 1997a; *Callot et al.*, 2000]. Moreover, *Marticorena et al.* [1997a] indicated that in the border of the hamadas of the north Sahara, where precipitation rates reach 80 to 100 mm.yr^{-1} [*Dubief*, 1963], the surface is characterized by a small stony cover and a large proportion of fine soil material. They also mention that 150 km further south, the mean annual precipitation does not exceed 40–50 mm, the surfaces are then almost covered by gravels, pebbles and stones. However, coarse sand generally prevails in these soils [*Marticorena et al.*, 1997a]. Both daïas and sebkhas (observed in the plains and in the endorheic depressions) generally represent small units of metric to kilometric surface scales [*Callot et al.*, 2000], except for specific cases such as the Chott Jerid in south Tunisia or the Bodélé Depression located in north Chad. However, these small units need to be properly described since their soils are rich in aggregates constituted of fine clay particles and have a high dust emission potential. Up to 2 different soil types are thus attributed to each quarter of square degree, in particular to represent small surface units such as the silty and salty depressions.

[42] Following *Marticorena et al.* [1997a] and *Callot et al.* [2000], the coarse medium sand (CMS) or coarse sand (CS) soils are associated with large and localized landscape units, such as the regs and hamadas. Combinations of fine and coarse sand (FS and CS) are associated to dune fields and are thus present over the main ergs. Small surface fractions of these two sand categories and of medium sand (MS) spread over the entire desert, and correspond to mobile sand sheets [*Marticorena et al.*, 1997a]. The silty fine sand (SFS) corresponds to ancient alluvial or fluvial depressions and is mainly concentrated on the northern desert margin, where the precipitation rates were sufficient in the past to produce such deposits [*Marticorena et al.*, 1997a]. The silty fine sand (SFS) and the medium silty sand (SMS) are thus attributed to local areas of daïas. The salty soils (SEM) constitute also minor soil types in the studied area, except for the Chott areas of Tunisia and Algeria. However, small surface units with high clay content are documented, since they can constitute intense local dust sources often referred to as "hot spots".

[43] Finally, 6 of the identified soil categories correspond to surfaces defined a priori as nonerodible, i.e., that cannot emit a significant amount of mineral dust (clayey soils, mountains, rocks or urban areas, rivers or large water plans, cultivated and irrigated lands, sea and ocean).

3.1.2.2. Smooth Roughness Length z_{0s}

[44] As mentioned before, the smooth roughness length (z_{os}) has to be characterized to describe the drag partition between the roughness elements and the erodible surface. Following *Marticorena et al.* [1997a], z_{os} is assumed to be $1/30$ of the coarser mass median diameter of the dry soil size distribution, except if the roughness length derived from POLDER-1 is lower. In this case, the surface is considered as a smooth surface where no drag partition applies ($z_{os} = Z_0$) and for which the characteristic aerodynamic roughness is the *PC* derived value.

3.1.3. Soil Texture

3.1.3.1. Saharan Soil Texture

[45] The north African soil database developed by *Marticorena et al.* [1997a] and *Callot et al.* [2000]

Table 2. Statistical Parameters of the Dry Soil Size Distributions for Soils of the North of Africa [*Marticorena et al.*, 1997a]: Median Diameter ($D_{med,i}$), Standard Deviation (σi), and Mass Fraction (Pi)

	Population 1			Population 2			Population 3		
Typology	Dmed1, μm	σ1	P1, (%)	Dmed2, μm	σ2	P2, %	Dmed3, μm	σ3	P3, %
Silty fine sand (SFS)	210	1.8	62.5	125	1.6	37.5	...	...	...
Medium sand (MS)	690	1.6	80	210	1.8	20	...	...	...
Coarse sand (CS)	690	1.6	100	...	...	...	...	...	...
Coarse medium sand (CMS)	690	1.6	90	210	1.8	10	...	...	...
Fine sand (FS)	210	1.8	100	...	...	...	...	...	...
Silty medium sand (SMS)	125	1.6	37.5	210	1.8	31.25	690	1.6	31.25
Moderately salty silt (SEM)	520	1.5	80	125	1.6	20	...	...	...
Highly salty silt (SEF)	520	1.5	92	125	1.6	8	...	...	...
Salt waste (SW)	125	1.6	50	520	1.5	50	...	...	...
Agricultural soil (AGS)	125	1.6	100	...	...	...	...	...	...
Salty fine sand (SES)	210	1.8	50	520	1.5	40	125	1.6	10
Silty coarse sand (SCS)	690	1.6	60	125	1.6	40	...	...	...

Table 3. Clay Percent of the Identified Mineralogical Populations of the North African Desert Soils [*Marticorena et al.*, 1997a]

Typology	Mineralogical Feature	% Clay
Alumino-silicated-silt	clay mineral dominant	9.7
Fine sand	quartz dominant	3.6
Coarse sand	quartz	0
Salts	salt and clay minerals	3.2

included an estimation of the clay content that can be used to retrieve α. However, the complete textural information is required to compute the moisture of the superficial soil layer.

[46] The clay content (defined in this case as the particle diameters < 5.8 μm) for each of the four populations (alumino-silicated-silt, fine sand, corse sand and salts) was estimated from analyses (wet sedimentation techniques and laser granulometry) of seven samples of arid soils [*Marticorena et al.*, 1997a] (Table 3).

[47] The clay content of a soil composed by a mixture of these four populations can be estimated as:

$$\%\ \mathrm{Clay}_{soil} = \sum_{\mathrm{i}} p_i \times \%\mathrm{Clay}_i \qquad (8)$$

where % $\mathrm{Clay_i}$ is the clay proportion of the population i, and $\mathrm{p_i}$ its mass fraction in the soil.

[48] Equation (8) is applied to compute the clay content of the 12 soil types reported in Table 4. To obtain the complete texture of the soils (% sand, % silt and % clay), we investigate the texture components measured for soils from the North of Africa. A data set of 18 texture measurements is compiled from samples collected in Mali [*Nickling and Wolfe*, 1994], Tunisia [*Lafon*, 2004], and Niger [*Valentin*, 1991; *Lafon*, 2004; *Valentin et al.*, 2004]. This data set covers a large range of clay contents (0 to 35%) and of geographical extend.

[49] By plotting the clay content as a function of the sand content for these soil samples, a significant linear relationship ($n = 18$, $r^2 = 0.85$) is obtained (Figure 2). We thus assume that the sand content can be reasonably estimated from the clay content for the north African desert soils using this empirical relationship, whatever the geographical origin of the studied samples. The complete soil texture of each studied soils is summarized in Table 4.

3.1.3.2. Residual Soil Moisture and Ratio of Vertical to Horizontal Flux

[50] The residual soil moisture (w', see equation (5)) and the ratio of vertical to horizontal flux (α, see equation (7)) are computed for the 12 soil types using their estimated clay content (Table 4). Following *Laurent et al.* [2006], it is relevant to compute α for each of the 12 soil types directly from their soil clay content. The computed α are higher than ones estimated by *Marticorena et al.* [1997a] based on the mean α values of the four reference populations reported in Table 3. For the various Saharan desert soils, α ranges from $1\ 10^{-6}$ $\mathrm{cm^{-1}}$ for the coarse sand to $2.0\ 10^{-5}$ $\mathrm{cm^{-1}}$ for the agricultural soil (Table 4). The α values are consistent with the measurements performed by *Gillette* [1979], and the estimations made by *Laurent et al.* [2006] for the soils of north-eastern Asian deserts (from $1.64\ 10^{-6}$ $\mathrm{cm^{-1}}$ to $3.93\ 10^{-5}$ $\mathrm{cm^{-1}}$).

3.1.4. Fraction of Erodible Surface, *E*

[51] The dust flux is directly proportional to the fraction of erodible surface E (equation (6)). This parameter corresponds to the fraction of the surface that is not covered by the roughness elements and thus exposed to wind erosion.

[52] Based on the database of estimated roughness elements cover rates and aerodynamic roughness lengths established by *Marticorena et al.* [1997a] and *Callot et al.* [2000], *Laurent et al.* [2006] showed that for the desert areas the fraction of erodible surface decreases roughly as a function of the roughness length (see equation (10)). For Z_0 smaller than $3\ 10^{-3}$ cm, *Laurent et al.* [2006] considered the desert surface as totally erodible. Following these authors, we estimate E as a linear function of the logarithm of Z_0, when Z_0 exceeds $3\ 10^{-3}$ cm:

$$\text{for } Z_0 < 3\ 10^{-3}\ \mathrm{cm} \qquad \mathrm{E} = 1 \qquad (9)$$

$$\text{for } Z_0 > 3\ 10^{-3}\ \mathrm{cm} \qquad \mathrm{E} = 0.7304 - (0.0804 \times \log_{10}(Z_0)) \qquad (10)$$

3.2. Meteorological Parameters

[53] The meteorological input data used for this study are extracted from the ERA-40 database of the European Center for Medium-range Weather Forecast (ECMWF). The ECMWF Re-Analysis (ERA-40) project produced a com-

Table 4. Texture (% Sand, % Silt and % Clay), Residual Moisture (w′) and Mean Flux Ratio (α) for the Soil Types Used for the Cartography Over the North of Africa

Typology	% Sand	% Silt	% Clay	w'	α , $\mathrm{cm^{-1}}$
Silty fine sand (SFS)	82.6	11.5	5.9	1.05	6.2E-06
Medium sand (MS)	94.2	5.1	0.7	0.12	1.2E-06
Coarse sand (CS)	95.8	4.2	0.00	0.00	1.0E-06
Coarse medium sand (CMS)	94.9	4.7	0.4	0.06	1.1E-06
Fine sand (FS)	87.7	8.7	3.6	0.63	3.0E-06
Silty medium sand (SMS)	85.1	10.1	4.8	0.84	4.4E-06
Moderately salty silt (SEM)	85.6	9.9	4.5	0.80	4.0E-06
Highly salty silt (SEF)	87.4	8.9	3.7	0.66	3.1E-06
Salt waste (SW)	81.3	12.2	6.5	1.16	7.4E-06
Agricultural soil (AGS)	74.0	16.3	9.7	1.78	2.0E-05
Salty fine sand (SES)	86.6	9.3	4.1	0.71	3.5E-06
Silty coarse sand (SCS)	87.1	9.0	3.9	0.68	3.3E-06

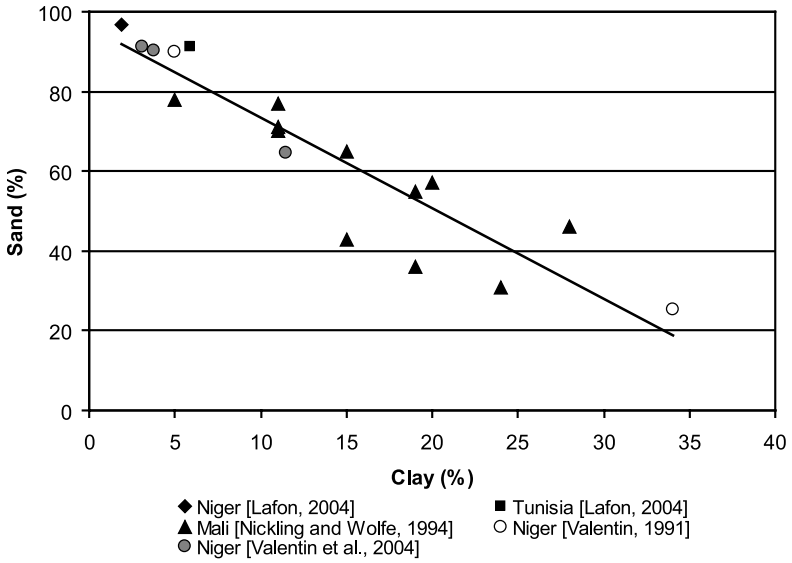

Figure 2. Sand (in %) versus Clay (in %) for soils of the north of Africa (n = 18, y = −2.28 x + 96.22, $r^2 = 0.85$).

prehensive global analysis for a 45-year period (from 1957 to 2002), making optimal use of a wide range of observing systems [*Betts and Beljaars*, 2003], especially satellite observations. Because of the lack of stations in desert environments the re-analysis meteorological fields using ground observations were less forced in these areas. A recent version of the ECMWF Numerical Weather Prediction system was used for the entire analysis period [*Uppala et al.*, 2004]. This surface meteorological database was used to successfully compute the mineral dust emissions over north-eastern Asia from 1996 to 2001 [*Laurent et al.*, 2006].

[54] The meteorological surface parameters used for the computation of dust emission fluxes are surface wind velocities, snow cover and soil moisture, the latter being computed using the daily precipitation and minimum and maximum air temperature, the albedo, and the geopotential. All the meteorological parameters are re-analyzed data products, except for the precipitation amount which are forecasted data.

[55] To compute the wind friction velocity, the ERA-40 surface wind fields at the ¼° × ¼° spatial resolution are used. These wind fields are instantaneous values of the two horizontal components u and v of the horizontal wind which are defined at 10-m height, for 00h00, 06h00, 12h00, and 18h00 UT. The wind velocity norm $(u^2 + v^2)^{1/2}$ is computed from u and v to obtain a 10 m wind velocity field.

[56] Moreover, the dust emission model includes the parameterization of the soil moisture influence on the erosion threshold proposed by *Fécan et al.* [1999]. The gravimetric soil moisture, w, is used as an input parameter. The soil moisture content is computed, like by *Laurent et al.* [2005, 2006], based on a water balance model [*Mougin et al.*, 1995] and using up to 14 soil layers as specified in the texture profiles [*Webb et al.*, 2000] associated to the global FAO soil texture map [*Zobler*, 1986]. The texture of the superficial soil layer (20 mm) is summarized in Table 4.

[57] Following *Laurent et al.* [2005], dust emissions are totally inhibited in the model when there is snow (i.e., snow depth > 0) on the surface. To account for the snow cover, the ERA-40 daily snow depth at the resolution of $^1/_4° \times {}^1/_4°$ are used. For the 6-year studied period, our simulations show that snow cover does not affect the mineral dust emissions from the Sahara.

[58] The simulated dust emissions presented and discussed further include the influence of soil moisture and snow cover.

4. Simulations of Saharan Mineral Dust Emissions

[59] Mineral dust emissions over the Sahara desert (extending from 16°N to 38°N and from 19°W to 40°E) are modeled based on the previously described surface and meteorological input data. U^*_t are computed for each grid box with a daily time step based on the POLDER-1 derived Z_0, the estimated z_{0s}, and the daily soil moisture. If the surface wind velocity exceeds the erosion threshold, an instantaneous dust flux is computed in each grid box with a 6-h time step from the surface wind velocity, the dry soil size distribution and α. The daily fluxes are estimated assuming that the instantaneous fluxes are representative of a 6-h interval. The daily fluxes ($g \cdot cm^{-2} \cdot d^{-1}$) are multiplied by the grid box surface to obtain the daily mass of emitted dust ($g \cdot d^{-1}$) for each ¼° × ¼° grid box. The surface of the grid box is estimated as a function of the latitude.

[60] As stressed in the introduction, there are no measurements of the Saharan dust emission to compare with the simulations. Our strategy is thus to use as much direct or indirect observations as available to test the simulated main trends. The capability of the simulations to locate the main dust sources is tested by comparing the location of simulated intense and frequent dust emissions to the Saharan dust sources identified in the literature. The simulated frequent dust sources are also compared to the regions where high dust indexes are frequently observed. We compare the seasonal cycle simulated over the western

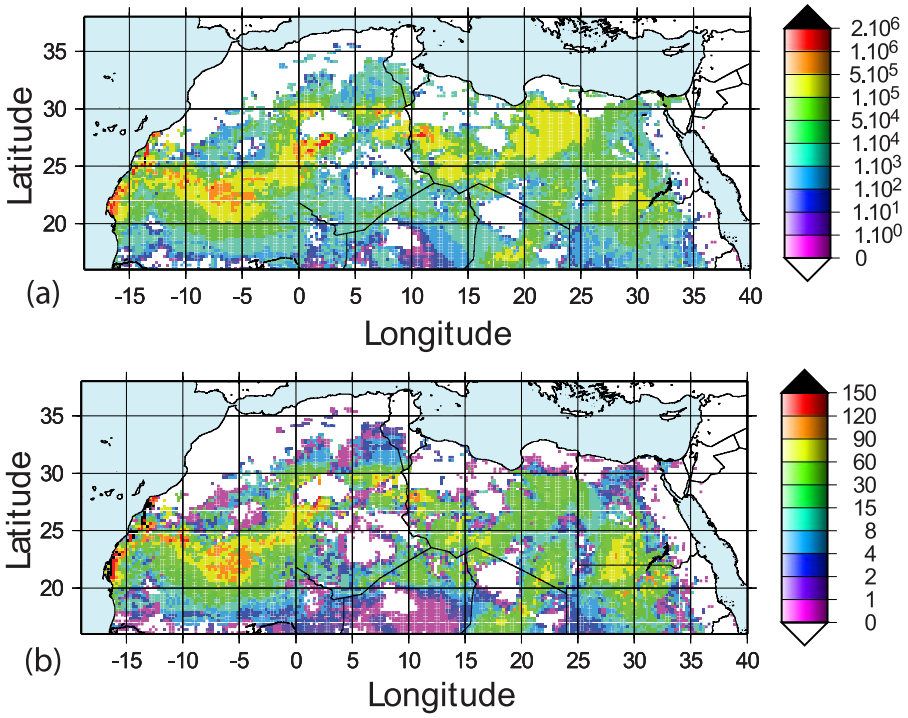

Figure 3. (a) Annual dust emissions (in Mg), and (b) annual number of dust events averaged on 6 years 1996–2001.

and eastern parts of the Sahara with the seasonal cycle of the frequency of horizontal visibility less than 5 km. We finally compare these seasonal cycles to the aerosol optical thickness measured in the main transport regions of Saharan dust: the North tropical Atlantic Ocean and the Mediterranean basin.

4.1. Simulations of the Main Saharan Dust Sources

[61] Figures 3a and 3b show the simulated annual dust emissions and number of daily dust events averaged over the 6-year simulated period (1996–2001). The number of dust events corresponds to the number of days the erosion threshold is exceeded. The two figures depict a similar pattern suggesting that the areas, where the dust events are the most frequent, are generally the most intense dust source areas. Nevertheless, we can note differences between the frequency and the intensity of the dust emissions for some of the simulated dust sources.

[62] The most frequent emissions (higher than 150 d per year) are simulated on the western Saharan coast (formerly the Spanish Sahara). The number of daily dust events is very high compared to the total dust amount emitted from this coastal area. Emissions are very frequent and intense in large areas of north-western Mauritania, on both sides of the border between the Mauritania and Mali (i.e., the southern part of the Chech Erg, 21°N–24°N; 8°W–2°W), in the south (~25°N, 13°E) and east (~28°N, 11°E) of Libya, on both sides of the border between the Egypt and Sudan (~23°N, 28°E), and in the region of the Bodélé Depression located south of the Tibesti massif (~18°N, 18°E). Inside these large source regions, intense dust emissions are simulated in small "hot spots", that often correspond to salty or silty depressions, for example the sebkhas of Mekherrane and Azzel Matti in Algeria (~26°N, 2°E). Moreover, the relative importance of different sources differs in frequency and in intensity, e.g., the Libyan Desert is a more intense source than the Sudan area but a less frequent one. These regions are characterized by low aerodynamic roughness (see Figure 1) and thus low erosion thresholds. However, this condition is necessary but not sufficient to simulate a dust source. In fact, the simulated dust emission frequency is controlled by the value of the erosion threshold compared to the distribution of the surface winds. The regions where dust emissions are intense correspond to the occurrence of high winds, the highest dust emissions being simulated for grid box including soils with high sandblasting efficiencies.

[63] All these source regions were identified as dust source regions by in situ [*Dubief*, 1953; *Kalu*, 1979; *D'Almeida*, 1986; *Middleton*, 1986] and/or satellite observations [*Brooks and Legrand*, 2000; *Middleton and Goudie*, 2001; *Prospero et al.*, 2002; *Washington et al.*, 2003]. This gives confidence in the capability of the simulations to reproduce the locations of the most intense and frequent dust sources.

[64] The results are also compared with semiquantitative indexes of the atmospheric aerosol content: the Absorbing Aerosol Index (AAI) derived from Earth Probe TOMS (Total Ozone Mapping Spectrometer) [*Herman et al.*, 1997; *Torres et al.*, 1998] and the Infrared Difference Dust Index (IDDI) derived from Meteosat observations in the thermal infrared [*Legrand et al.*, 1994, 2001].

[65] Following *Laurent et al.* [2005], the frequencies of AAI > 0.7 and of significant mineral dust events (corresponding to simulated dust flux > 10^{-10} g·cm^{-2} s^{-1}) are compared. As the AAI are available since July

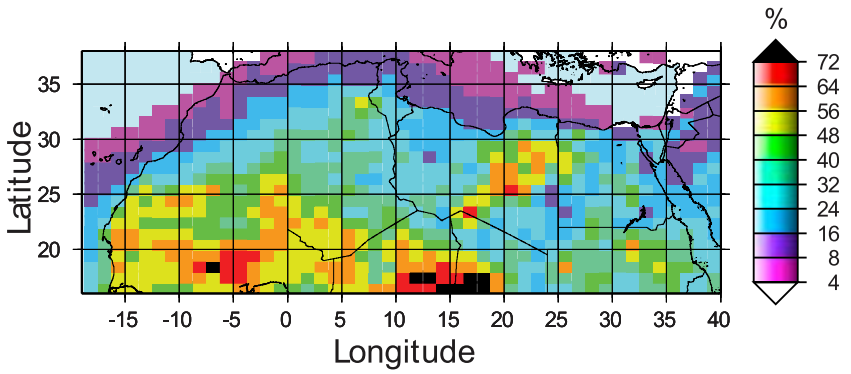

Figure 4. Map of the averaged annual frequencies of TOMS AAI > 0.7 (1997–1999).

1996 and a calibration drift is observed by mid-2000 (http://toms.gsfc.nasa.gov/aerosols/aerosols_v8.html, *technical note on the TOMS website*), the comparison is restricted to the 1997–1999 period. The AAI and the simulated dust event frequencies are computed from daily data only for the days for which TOMS observations are available. Some data are missing for several winter months (November and December 1997, December 1998, and January 1999). As a result, the comparison is less constrained for this season where dust emissions are low.

[66] Figure 4 presents the frequencies of AAI > 0.7 for the 1997–1999 period. Most of the simulated frequent source areas are also pointed out by the AAI, but with a different relative importance: regions around the border of the Mali and Algeria, the Bodélé Depression, the eastern Libya, the south Egypt and north Sudan, and small areas in Mauritania and in the western Saharan coast. The AAI suggest high dust event frequencies in the south of Mauritania and Mali (16°N–21°N), i.e., downwind of the simulated major dust source area located on both sides of the border between the Mauritania and Mali. In the south of the Sahara, the simulated dust emissions seem to be underestimated, especially in the region of the Bodélé Depression where the AAI frequencies are the highest in agreement with *Prospero et al.* [2002] and *Washington et al.* [2003].

[67] The simulated dust emissions are also compared with the IDDI derived from the Meteosat observations. A composite IDDI map at the ¼° × ¼° spatial resolution is produced from the initial data set at the 5 km × 5 km spatial resolution. A ¼° × ¼° pixel is considered as cloudy if more than 80% of the full resolution values are cloudy. It is classified as dusty if more than 50% of the initial IDDI values are higher than 25 radiometric counts (cts). Such a threshold corresponds to a horizontal visibility lower than 1 km [*Legrand et al.*, 1994, 2001; *Léon and Legrand*, 2003]. Because of frequent clouds, more than 30% of the data missed for the Algerian and Tunisian Coast and the western part of the south Sahara. The comparison is thus less forced in these areas. To make the comparison with the simulations consistent, the frequencies of significant mineral dust events (corresponding to simulated dust flux $>10^{-10}$ g·cm^{-2} s^{-1}) are computed only for noncloudy pixels.

[68] Figure 5 presents the frequencies of IDDI > 25 cts for the clear days of the period 1996–2001. The main active areas identified both by the IDDI and the simulations are: large areas in Mauritania and Mali, the south-west of Algeria and the area of the sebkhas of Mekherrane and Azzel Matti, the Bodélé Depression, and the north of Sudan. These sources were already evident from mineral dust atmospheric content climatology established using 10 years of Meteosat IDDI [*Brooks and Legrand*, 2000]. Surprisingly, the Algerian and Tunisian Coast presents high IDDI frequencies, which is not shown by the simulated dust emission or the frequency of high AAI maps. *Legrand et al.* [2001] indicated that the IDDI quality can be degraded for regions and periods with large cloudiness and atmospheric humidity and the results have to be considered with caution. This is possibly the case in this region where the cloud

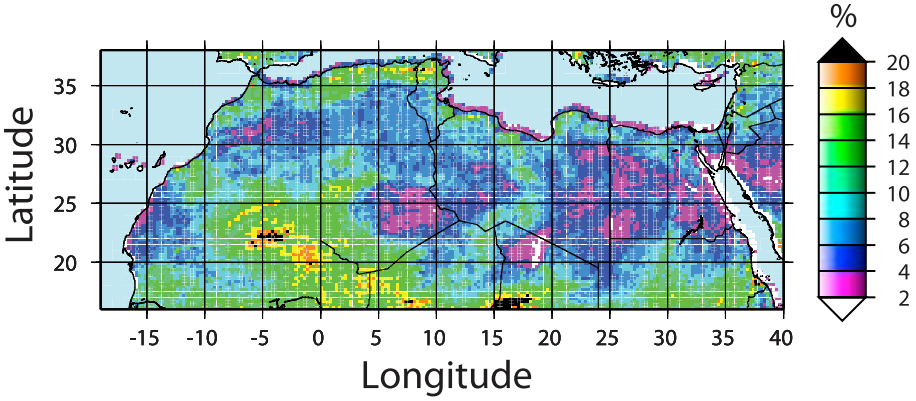

Figure 5. Map of the averaged annual frequencies (1996–2001) of Meteosat IDDI > 25 cts.

cover frequency is high. In addition, the Libyan Desert is not detected as a dust source by the IDDI unlike the information delivered by the simulations and the AAI. The IDDI point out coastal dust sources in the north of Western Sahara, but not in the southern coastal part, as indicated by the simulations and the AAI. In agreement with the AAI and *Brooks and Legrand* [2000], high IDDI frequencies are also located south of 20°N. They are particularly high in the region of the Bodélé Depression. As already mentioned the model does not simulate such high dust emission frequencies in the southern Sahara.

[69] In conclusion, the locations of the simulated dust source areas are generally in agreement with the satellite dust indexes. Nevertheless, it is difficult to conclude on the relative importance of the identified dust sources. Indeed, the two dust indexes used for the comparison sometimes point out different source areas. However, the simulations seem to under- or over-predict the dust emissions for some specific areas identified as dust sources by the two indexes. These cross-comparisons point out the present limits of the satellite dust indexes and their limitation to be used as validation tools for modeling studies of the mineral dust emissions.

[70] The high AAI observed in the south of Mauritania and Mali are shifted downwind of the major dust source area pointed out by the simulations and the IDDI. Part of the observed spatial shift can be explained by the AAI sensitivity to the height of the dust transport. To test the implication of this sensitivity, *Yoshioka et al.* [2005] computed the AAI from mineral dust concentrations simulated by a global model. They found that, in the area of the Bodélé Depression, the higher simulated AAI are not located over the source area but further west. For a homogeneous dust concentration the simulated AAI increase as the dust plume rises. As a result, the maximum AAI can be shifted from the maximum dust emission area in the direction of the prevailing wind.

[71] Dust source areas are located in the eastern Libyan Desert both in the simulations and on the AAI maps but are not pointed out by the IDDI. Conversely sources are simulated in the sebkhas of Mekherrane and Azzel Matti in agreement with the IDDI but does not appears at all in the AAI maps. These discrepancies suggest that some sources can be missed when using the satellite dust indexes. This can be partly explained by the sensitivity of these two indexes to different characteristics of the dust plumes, but also by differences in their spatial resolution.

[72] Both the AAI and IDDI tend to suggest that the model overestimates the dust emission frequencies along the coast of the Western Sahara. This area was identified as a dust source region by *Dubief* [1953] and *D'Almeida* [1986]. Synoptic observations of dust storms and sand drift measured at the Nouakchott meteorological station (located on the Mauritanian coast) also show an intense local aeolian activity in this region [*Dumay et al.*, 2002]. From 1996 to 2000, the annual number of days with drifting sand is of the order of 100, while the annual number of dust storms is five times less frequent. It tends to confirm that the erosion threshold is frequently exceeded allowing local sand movement, but that intense local dust emissions are quite unusual (~5% of the time in the year). The simulated pattern of dust emissions of low intensity but high dust event frequencies appears realistic regarding the observations. The simulation suggests that the surface wind velocity often exceeds the erosion threshold but is only slightly higher. To reach a better quantitative agreement, a higher precision on the erosion threshold and of the surface wind fields would thus be necessary in this area.

[73] The AAI and the IDDI converge to point out the Bodélé Depression as one of the most active dust sources. It is clear that the model under predicts the dust emissions in this area. The surface database used to perform the simulations describes this area as a sandy surface with low aerodynamic roughness lengths and thus low erosion thresholds (range from 7 to 8 m s^{-1} for the smoothest areas). Recent exploration of this area (BOdélé Dust EXperiment, 2005) revealed very complex surface features and in particular the presence of diatom deposits, sand dunes and dunes made of sand-sized pellets of diatoms [*Warren et al.*, 2007]. From direct observations, *Warren et al.* [2007] argued that dust emission processes in this area involve the "auto-abrasion" of saltating flakes of diatomite, occurring either in collision with each other or with the bed, saltating quartz sand being not so much involved in dust production. Our soil typology does not include a specific population representing the fraction of the soil that is composed of diatoms. In our data set, the soil of the ¼° × ¼° grid box including the explored part of the Bodélé Depression (about 8 × 7 km, see *Chappell et al.* [2008]) is composed of silty fine sand soil (D_{med1} = 210 μm, σ_1 = 1.8, P_1 = 62.5; and D_{med2} = 125 μm, σ_2 = 1.6, P_2 = 37.5, see Table 2) and coarse sand (D_{med1} = 690 μm, σ_1 = 1.6, P_1 = 100, see Table 2). These size ranges are consistent with the two modes (200 μm and 800 μm) identified in surface samples by *Chappell et al.* [2008].

[74] Consequently, the low simulated dust emission frequencies can only be due to the fact that the surface wind velocities are most of the time lower than the erosion threshold. The Bodélé Depression is located southwest of two mountain ranges, the Tibesti (3410 m) and the Ennedi (1310 m). This geographical location induces a channeling effect leading to strong surface winds. *Washington and Todd* [2005] identified a low level jet in the Bodélé and pointed out the difficulty of global meteorological models to reproduce this phenomenon. *Bouet et al.* [2007] showed how a regional meteorological model used at 10 km × 10 km spatial resolution was able to reproduce the intensity of the measured surface wind velocities and the order of magnitude of the measured aerosol optical depth. They indicated that using a spatial resolution of 50 km × 50 km instead of 10 km × 10 km would lead to an underestimation of the dust emissions of more than 40%. These elements strongly suggest that the surface wind fields used in this work are not able to reproduce high surface wind velocities in the Bodélé Depression. The underestimation of the simulated dust emissions from this region can be considered as the main uncertainty in our estimations of the emissions over the studied area. Our estimations must then be considered as a minimal value of the Saharan dust emissions. An improvement of this work would need better resolved surface wind fields in the area of the Bodélé Depression, similar to the ones produce by regional meteorological models but for climatological timescales.

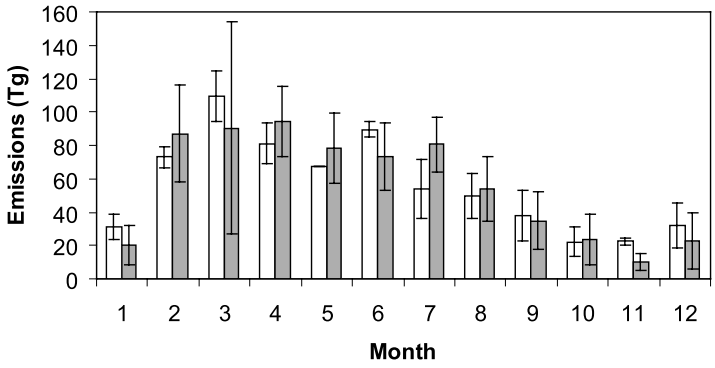

Figure 6. Averaged monthly dust emissions (in Tg) simulated for the Sahara desert (this work: averaged from 1996 to 2001, grey bars) and estimated by *D'Almeida* [1986] (average for 1981 and 1982; white bars). The error bars represent the standard deviation associated to the mean value.

4.2. Seasonal Cycle

[75] The simulations are now further analyzed by examining the seasonal cycle of the dust emissions. The monthly dust emissions are computed for the 6-year simulations and over the whole simulation domain (Figure 6, grey bars). The simulated dust emissions exhibit a clear seasonal cycle with a maximum in spring, a secondary peak in summer, and a minimum in autumn. The monthly standard deviation does not exceed 30 Tg, excepted in March (70 Tg). This high-standard deviation in March is mainly due to extremely high dust emissions in March 1998 (205 Tg) that shift the average value from 65 to 90 Tg. When compared to the monthly average dust emissions, the standard deviation is relatively higher in winter.

[76] This seasonal cycle is compared to the estimation proposed by *D'Almeida* [1986] based on in situ observations of aerosol optical thickness, mass concentrations and visibility measurements from several meteorological stations located in the North of Africa. These monthly emissions, averaged for 1981 and 1982 over the whole Sahara, are presented in Figure 6 (white bars). The temporal variations of the estimated and simulated dust emissions are very similar: the highest dust emissions occur in spring and the lowest in autumn. The order of magnitude of the simulated monthly dust emissions is also consistent with the emissions estimated from observations. The monthly dust emissions estimated by *D'Almeida* [1986] vary from 20 Tg (in October and November) to 110 Tg (in March), while the simulated emissions vary from 10 Tg (in November) to 95 Tg (in April). The differences between the estimated and simulated monthly emissions are of the order of 20%, except for July and the 3 months of low emissions (January, November, and December).

[77] To further study the seasonality of the dust emissions over the Sahara, we compute the monthly dust emissions in the western Sahara (16°N–38°N; 19°W–14°E) and the eastern Sahara (16°N–38°N; 14°E–40°E). Note that these two areas have respectively 4.5 millions km^2 and 4 millions km^2. As a result, lower dust emissions are expected over the eastern Sahara. The monthly dust emissions and the relative occurrence of dust emission events averaged from 1996 to 2001 for the western and eastern Sahara are displayed respectively in Figures 7a and 7b. The two areas have a clear but different seasonal cycle.

[78] The emissions from the western Sahara are characterized by a maximum in summer (June and July), and a minimum at the end of autumn (November and December). A second peak is simulated in February. Both the emissions and the occurrence of dust events have the same seasonal cycle and are highly correlated (r^2 = 0.98 using a linear regression). This correlation suggests that the dust emission maximum is due to a simultaneous increase of the number and the intensity of the dust emission events. The summer maximum is consistent with the results from *Engelstaedter and Washington* [2007]. On the basis of an analysis of the TOMS AAI between 1980 and 1992, they pointed out that June is the peak month in the western African dust cycle, coinciding with the crossing of the convergence zone on its northward bound over the dust "hot spots".

[79] In contrast, dust emissions from the eastern Sahara are highest in spring, with a secondary maximum in late summer and beginning of autumn. The seasonal cycle of the dust emission occurrence is similar but the maximum tends to occur 1 month earlier in spring. The relative occurrence is not linearly correlated with the intensity of the dust emissions. In spring, the relative dust emissions are high compared to the dust event occurrences. Typically the dust event occurrences are comparable in March and May while the dust emissions are almost twice higher in March than in May. This difference suggests the occurrence of few but intense dust events in March over the eastern Sahara. In the summer and autumn, the relative occurrences are much higher than the relative dust emissions, suggesting numerous dust events of low intensity. Compared to the western Sahara, the standard deviation of the monthly dust emissions in Tg is higher for the eastern Sahara. It points out the large variability of the eastern Saharan emissions.

[80] At the present time, there is no unquestionable quantitative observation of the dust content and the dust emissions over the Sahara that would allow the validation of the seasonal cycle. However, indirect observations of emitted and transported dust can be used to test whether the simulations are realistic or not, at least in terms of temporal variations.

[81] In particular, the visibility less than 5 km measured in the meteorological stations of North of Africa allow to determine the general trend of the dust variability [*Mahowald et al.*, 2007]. The relative occurrence of simu-

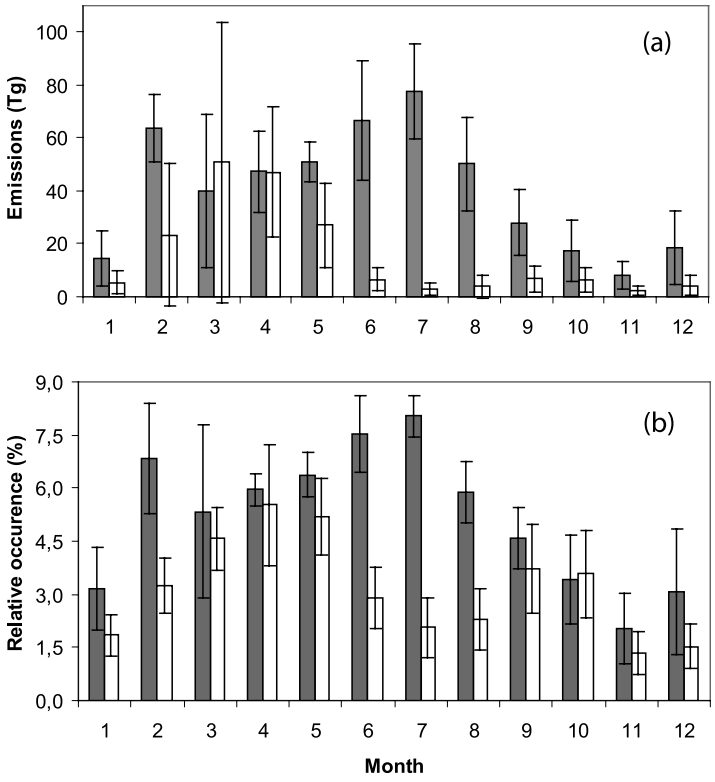

Figure 7. (a) Averaged monthly dust emissions (1996–2001) in Tg, for the western Sahara (in grey) and the eastern Sahara (in white). (b) Average monthly relative occurrence of dust emissions (1996–2001, simulated with 6-h step) in %, for the western Sahara (in grey) and eastern Sahara (in white). The error bars indicate the standard deviation associated to the mean value.

lated dust emissions is compared to the fraction of observations with visibility less than 5 km (as VIS5 computed by *Mahowald et al.* [2007]) for the western (Figure 8a) and for the eastern (Figure 8b) part of the Sahara for the 1996–2001 period. The mean monthly VIS5 are averaged for all the meteorological stations included between 13°N–38°N and 19°W–14°E for the western part of the Sahara, and between 13°N–38°N and 14°E–40°E for the eastern Sahara (the complete data set is presented by *Mahowald et al.* [2007]). For the western Sahara, the general trend of the seasonal cycle appears similar except for the relative intensity of the two maxima. In fact, contrary to the mean monthly occurrences of dust emissions, the mean monthly VIS5 are the highest in February and March but with a large variability indicated by the standard deviation associated to the mean value, and they present a more constant second maximum in summer. This relative difference can partly be explained by the fact that the stations located in the south of the western Sahara are also downwind of the eastern sources of dust emissions (e.g., the Bodélé Depression). For the eastern Sahara, a very clear and marked seasonal cycle is obtained both by the mean monthly occurrences of dust emissions and the mean monthly VIS5. This tends to confirm that the dust emissions of the eastern Sahara are the highest in spring. We can notice that the simulated occurrences of dust emissions seem to be under estimated during the winter time when some eastern dust sources like the Bodélé Depression are active.

[82] Moreover, dust transports over the North Atlantic Ocean [*Chiapello*, 1996; *Kaufman et al.*, 2005] and the Mediterranean Sea [*Moulin et al.*, 1998] were investigated based on ground measurements and satellite observations. A part of the variability of the mineral dust content in these transport regions is due to the variability of the dust sources.

[83] *Chiapello* [1996] showed that the Aerosol Optical Thickness (AOT) derived from Meteosat for the year 1987 over the Cape Verde Islands exhibited a seasonal cycle marked and characterized by a maximum in summer. For the period 2000 to 2003, the AOT measured at the ground level using a Sun photometer from the AERONET network and the ones derived from the MODIS observations over the Cape Verde Islands [*Kaufman et al.*, 2005] confirmed this seasonal cycle. Figure 9 shows the monthly AOT measured at the AERONET station of the Cape Verde Islands averaged for 1996–2001 and the simulated monthly dust emissions averaged over the western Sahara for the same period. The monthly AOT exhibit the same cycle than the simulations with a maximum in summer, a secondary peak in February–March and a minimum in autumn. These results tend to confirm the validity of the simulations and suggest that most of the dust transported over the Cape Verde islands originates from the western Sahara.

[84] *Moulin et al.* [1998] investigated the spatial and temporal variability of the AOT over the Mediterranean basin based on Meteosat observations. On Figure 10, we compare, season by season, the AOT derived for a 10-year climatology (1984–1994) over the western part of the Mediterranean basin (resp. eastern part) to the simulated dust emissions for the western Sahara (resp. eastern Sahara).

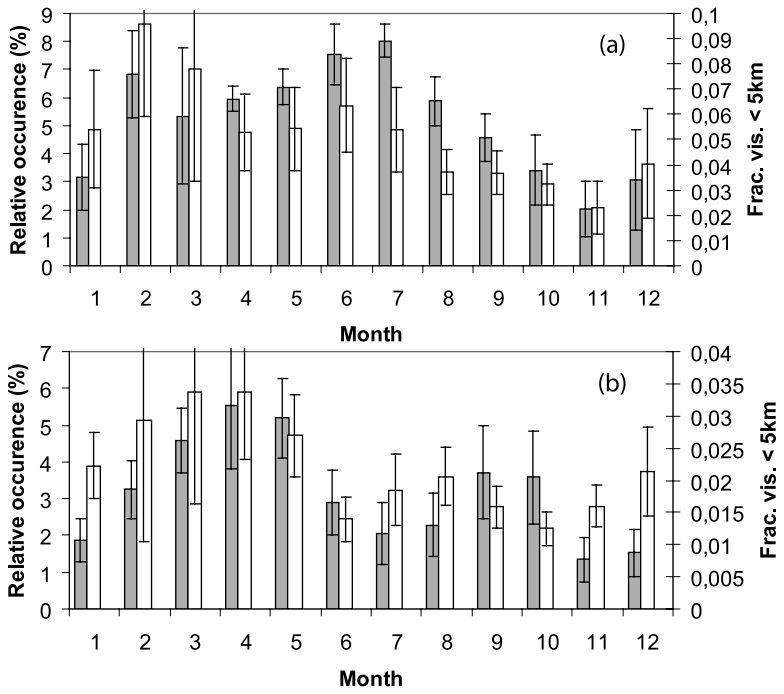

Figure 8. Average monthly relative occurrence of dust emissions (1996–2001, simulated with 6-h step) in % (in grey), and the fraction of observations with visibility less than 5 km (in white) [*Mahowald et al.*, 2007], for the (a) western Sahara and (b) eastern Sahara. The error bars indicate the standard deviation associated to the mean value.

The AOT exhibit a maximum in summer and a minimum in autumn over the western Mediterranean Sea. For the eastern Mediterranean Sea, the highest values of the AOT are observed in spring and remain quite high in summer, the minimum being observed in autumn. The simulated dust emissions reproduce remarkably well the differences between the western and eastern Mediterranean basin in the observed seasonal cycle of dust (Figure 10).

[85] *Moulin et al.* [1998] indicated that the high AOT measured in April in the Central and eastern Mediterranean Sea were due to dust emissions from the Libyan deserts [*Dayan et al.*, 1991; *Kubilay and Saydam*, 1995] and from Egypt [*Dayan*, 1986]. The high AOT observed in June over the central Mediterranean Sea were mainly attributed to dust emissions of the north-western part of Africa [*Moulin et al.*, 1998]. The high AOT observed in August over the western part of the basin could be due to north African emissions, as suggested by *Bergametti et al.* [1989a, 1989b], based on backward air masses trajectories associated with aerosol sampling in Corsica.

[86] Finally, our simulations suggest a difference in the seasonal cycle of dust emissions between the western and eastern parts of the Sahara. These simulated seasonal cycles are consistent with the observed general trend of the seasonality of dust observations from the meteorological

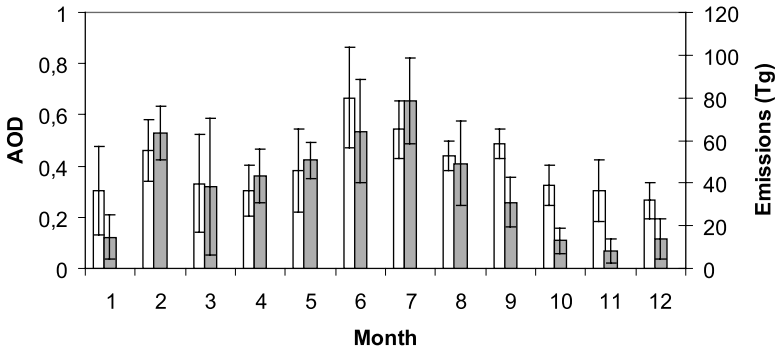

Figure 9. Monthly aerosol optical depths (440 nm) over Cape Verde Islands averaged over the period 1996–2001 (except for March 1998 to December 1998 and April 1999; original level 2 data from AERONET-PHOTONS) in white; and monthly simulated dust emissions for the western Sahara averaged over the same period in grey. The error bars indicate the standard deviation associated to the mean value.

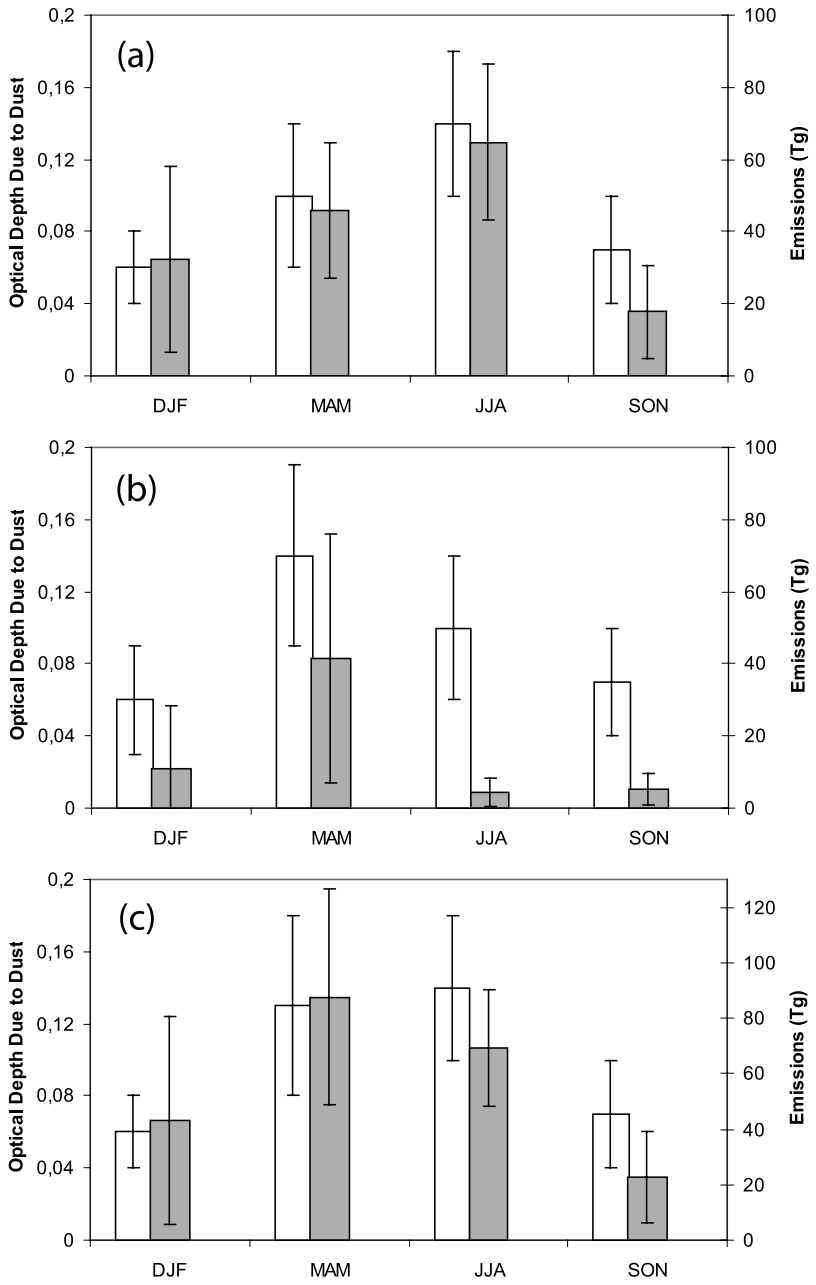

Figure 10. Mean seasonal optical depth due to dust (in white, data from *Moulin et al.* [1998]) and simulated mineral dust emissions in Tg (in grey), respectively (a) over the western Mediterranean Sea and from the western Sahara, (b) over the eastern Mediterranean Sea and from the eastern Sahara, and (c) over the total Mediterranean Sea and from the Sahara. The error bars indicate the standard deviation associated to the mean value.

stations and of dust transported over the North Atlantic Ocean and the Mediterranean basin.

4.3. Annual Dust Emissions and Inter-Annual Variability

[87] The averaged annual dust emissions from the Sahara over the 6-year simulated period is nearly 670 Tg ± 60 Tg (Table 5). Annual dust emissions vary from 585 Tg in 1999 to nearly 760 Tg in 1998. The simulated dust emissions are in agreement with the previous estimations summarized by *Goudie and Middleton* [2001] and ranging between 130 and 760 Tg a^{-1}, in particular with ones estimated by *D'Almeida* [1986] (630–710 Tg·a^{-1} for 1981 and 1982), and by *Callot et al.* [2000] (∼760 Tg·a^{-1} for 1990 to 1992).

[88] Our simulations are also consistent with the estimations of dust emissions at global scale which range from 1000 to 3000 Tg a^{-1} [*Tegen and Fung*, 1994; *Duce*, 1995; *Mahowald et al.*, 1999; *Mahowald and Luo*, 2003; *Tegen et al.*, 2004]. With a mean value close to 670 Tg a^{-1}, our simulations suggest that the Saharan emissions could represent 20 to 65% of the global mineral dust emissions.

Table 5. Annual Dust Emissions Simulated From 1996 to 2001 (in Tg), for the Whole Sahara Desert, the Western Sahara, and the Eastern Sahara

Emissions	Sahara (in Tg)	Western Sahara (in Tg)	Eastern Sahara (in Tg)
1996	699	420	279
1997	627	480	147
1998	759	505	255
1999	585	479	106
2000	643	486	157
2001	700	524	176
Mean	669	482	187
σ	62	35	67

[89] The simulated Saharan dust emissions are 2 or 3 times higher than the emissions simulated in the same conditions for the north-eastern Asian deserts (240 Tg) [*Laurent et al.*, 2006]. However, the Saharan dust emissions are regular over the studied period with a mean interannual variability close to 10%, while the north-eastern Asian emissions exhibit a large interannual variability (about 50% on average). With more than 900 Tg·a^{-1}, the north African and north-eastern Asian emissions could represent 30 to 90% of the global mineral dust emissions.

[90] Annual dust emissions from the western part of the Sahara (480 Tg ± 35 Tg) and from the eastern part (187 Tg ± 67 Tg) have been computed (Table 5). The western and eastern parts of the Sahara do not exhibit the same interannual variability. In particular, the highest and weakest annual emissions are not simulated the same years for the western Sahara (maximum in 2001 and minimum in 1996) and for the eastern Sahara (maximum in 1996 and minimum in 1999). The variability of the annual emissions reaches 60% for the eastern Sahara and is much weaker for the western Sahara (20% at the most). The western Sahara appears as a steady dust source over the 6-year simulation. These results point out the fact that western and eastern Saharan dust emissions exhibit different temporal dynamics suggesting that they are controlled by different and possibly independent meteorological systems.

[91] Figure 11 presents the monthly emissions in Tg and the relative occurrence of dust events over the western Sahara from January 1996 to December 2001. The largest monthly emissions are obtained when the dust events are the most frequent. During the 6-year simulated period a maximum (~100 Tg per month) is generally observed in summer and a second one in February, except for 1997 for which the maximum is simulated in late winter and spring. Except for this specific year, the weakest emissions are simulated in late autumn and at the beginning of the winter (i.e., from November to January).

[92] The interannual variability of the eastern Saharan dust emissions is very pronounced and mainly related to

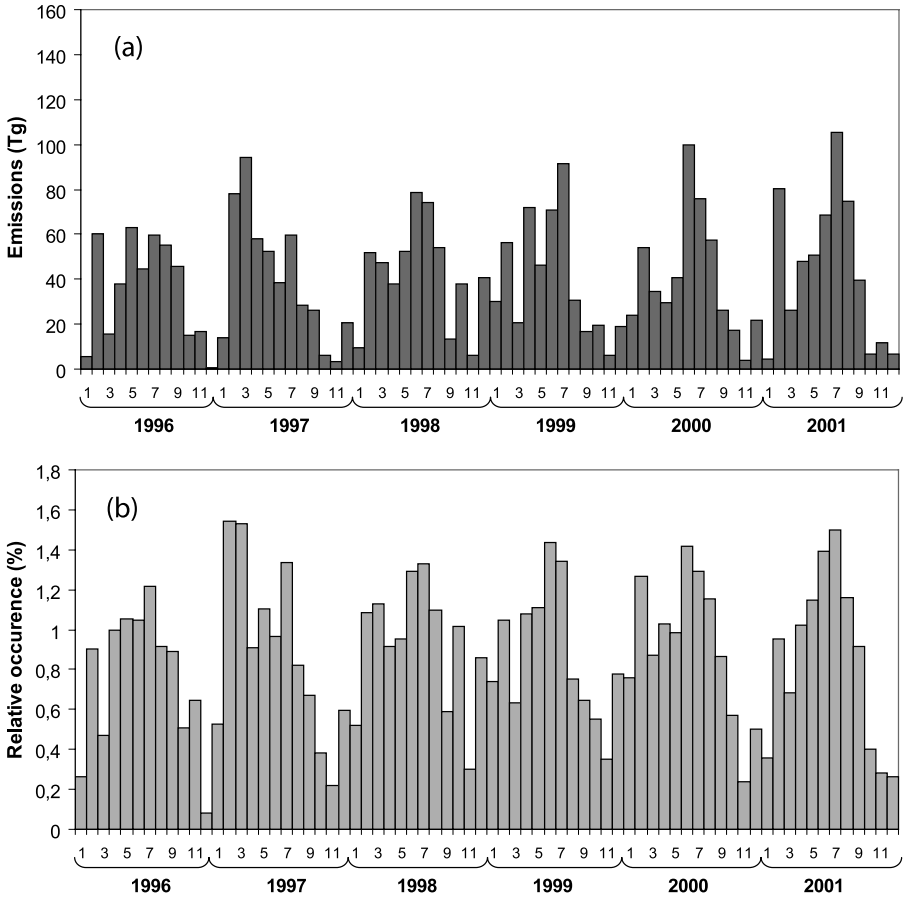

Figure 11. (a) Monthly dust emissions (in Tg), and (b) monthly relative occurrence of dust emissions (simulated with a 6-h time step), for the western Sahara (January 1996 to December 2001).

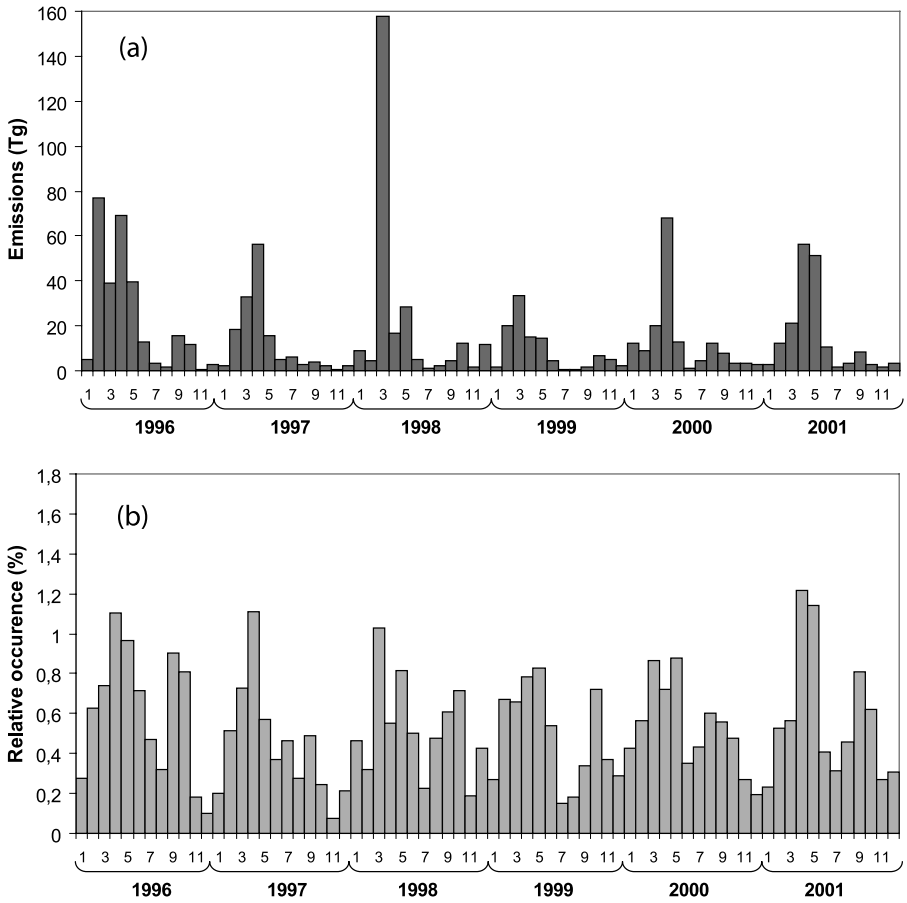

Figure 12. (a) Monthly dust emissions (in Tg), and (b) monthly relative occurrence of dust emissions (simulated with a 6-h time step), for the eastern Sahara (January 1996 to December 2001).

changes in the intensity of spring dust emissions (Figure 12). In contrast, the relative occurrences of dust events exhibit quite a regular pattern over the 6 years. In March 1998, the dust emissions (158 Tg) are 3 times higher than dust emissions averaged over the 6 years in March (50 Tg), while the relative occurrence of dust events in 1998 is not significantly higher than the 6-year average. The same variability is observed in February 1996, for which the monthly dust emissions (77 Tg) are 3 times higher than the 6-year average (23 Tg). The intensity and the frequency of dust events are clearly not correlated for the studied period. The high interannual variability should be explained by few sporadic and very intense dust events. The emissions from the eastern Sahara seem to account for most of the interannual variability of the whole Saharan emissions.

[93] To estimate the influence of the soil moisture on the annual and seasonal dust emissions, simulations are also performed without taking into account the increase of the erosion thresholds due to the soil moisture. Results of the two simulations (with or without the soil moisture influence) are summarized in Table 6. During the most intense period of dust emissions, in spring and summer, the influence of the soil moisture is weak (between 0.6 to 4%). Emissions occurring during the months of December, January, February, and March are the most affected by the soil moisture influence, but the global decrease on Saharan dust emissions does not exceed 6%.

[94] However, this decrease of several percents on dust emissions over important dust sources can lead to a decrease of the emitted dust of several ten thousand tons per year. Such a notable decrease can be observed on the western Coast, in Mauritania, in north Algeria and south Tunisia, in south and east Libya, and in north Egypt. Moreover, accounting for the influence of the soil moisture, the dust emissions decrease by more than 70% in a

Table 6. Relative Decrease in the Simulated Monthly Dust Emissions During the Period 1996–2001 Due to the Influence of the Soil Moisture for the Western Sahara, the Eastern Sahara, and the Whole Studied Area

	Relative Decrease in Dust Emissions Due to Soil Moisture, %		
	Western Sahara	Eastern Sahara	Total
Jan	6.4	3.7	5.3
Feb	1.6	6.3	2.7
Mar	8.0	1.7	4.0
Apr	1.8	0.4	1.2
May	0.8	0.3	0.6
Jun	1.2	0.0	1.0
Jul	1.5	2.3	1.5
Aug	1.3	0.9	1.3
Sep	1.9	0.1	1.6
Oct	1.8	0.2	1.4
Nov	2.9	1.8	2.5
Dec	10.4	4.5	5.7

few localized areas in north Morocco, Algeria, Libya and Egypt. This suggests that soil moisture can partly control and limit the dust emissions in the northern desert margin, where the precipitation rates are higher.

[95] For the 6-year simulation, due to very low precipitation over the studied area which contains the hyper arid areas of the North of Africa, the soil moisture does not noticeably affect the Saharan dust emissions, their seasonal cycle, or their interannual variability.

5. Conclusion

[96] The subdaily mineral dust emissions of the North of Africa are simulated with a $1/4° \times 1/4°$ spatial resolution from 1996 to 2001. Both the quality of the physical model used without any adjustment factor and the relevance of the new surface and soil databases developed in this work allow a deeper analysis of the mineral dust emissions at the continental scale. The main input of this work comes from the use of these new surface and soil data with an optimized spatial resolution. Surface parameters controlling dust emissions are derived from experimental data or satellite observations, without any a priori hypothesis on the efficiency of the different surface types to produce mineral dust. The method developed to produce this data set allows representing large source areas such as the Libyan Desert but also of small areas of intense dust emissions ("hot spots"). In addition, the temporal resolution of the simulations respects the sporadic nature of dust emissions and allows reproducing nonfrequent and unusually intense dust events and then the interannual variability of the dust emissions. The results thus illustrate how well our current knowledge, of the physic dust production processes and of the surface properties in desert areas, allows to simulate the dust emissions.

[97] The main Saharan dust sources identified for the 6-year simulation are in agreement with the previous reference works and satellite aerosol indexes (TOMS AAI and/or Meteosat IDDI). The simulated emissions are the most frequent on the western Saharan coast, and are very high in a large area between Mauritania and Mali. Hot spots such as the sebkhas Mekherrane and Azzel Matti are also intensive sources of emissions. Dust sources are simulated in the Bodélé Depression, the north-eastern part of Libya, south of Egypt and north of Sudan. Moreover, we note that the relative importance of the different sources can differ in frequency and in intensity. For example, the Libyan Desert is a more intense source than the Sudan area but a less frequent one.

[98] The mineral dust emissions from the western Saharan coast are difficult to simulate correctly. Indeed, the surface wind velocities are frequently close to the erosion thresholds, requiring a very high accuracy for both the erosion thresholds and the surface wind velocities. Moreover, simulated emissions from the Bodélé Depression, which is considered at the present time as the most intense source [e.g., *Prospero et al.*, 2002], are underestimated. This is due to a deficiency in the surface wind velocity derived from global meteorological models which are not able to correctly account for the specific topography of the region. An improvement of this work would need better resolved surface wind fields in some specified areas where their description is not yet accurate enough.

[99] Well-marked seasonal cycles of the dust emissions are simulated, with a maximum in summer for the western Sahara and in spring for the eastern Sahara, in agreement with the visibility less than 5 km measured in the meteorological stations of the North of Africa and the AOT. Western and eastern Saharan dust emissions exhibit different temporal dynamics which could be controlled by different and independent meteorological systems. A high variability of the dust emissions of the eastern Sahara is also pointed out and not correlated with an increase of the occurrence of dust events. For example, in February 1996 and in March 1998 the monthly dust emissions exceed of more than a factor of 3 the dust amount averaged over the 6 years for these months.

[100] The averaged annual dust emissions from the Sahara over the 6-year simulated period is 670 Tg ± 60 Tg. These simulated Saharan dust emissions are two or three times higher than the emissions simulated in the same conditions for the north-eastern Asian deserts (240 Tg) [*Laurent et al.*, 2006]. Our simulations tend to confirm that the Sahara is the major terrestrial source of mineral dust and could represent up to 65% of the global emissions. The annual emissions present a weak interannual variability, 10% on average for the 6-year study. The interannual variability of dust emissions is mainly observed in the eastern Sahara (106 to 279 $Tg \cdot a^{-1}$) while the emissions from the western Sahara are more regular over the studied period (420 to 524 $Tg \cdot a^{-1}$). The effect of the precipitation being negligible on the dust emissions except for few localized areas on the western Saharan coast, in north Morocco, Algeria, Libya and Egypt, the interannual variability of the emissions is controlled by the surface wind velocities used as input data of the model.

[101] **Acknowledgments.** We thank Bernadette Chatenet, Didier Tanré and the PHOTONS project for their efforts in establishing and maintaining the Capo Verde site. Results presented in this paper were obtained using data from the Centre National d'Etudes Spatiales (CNES) acquired by POLDER-1 instrument onboard NASDA's ADEOS. The Earth Probe TOMS AI was made available by the NASA/GSFC TOMS Ozone Processing Team (OPT). We also would like to thank the reviewers for their helpful comments.

References

Alfaro, S. C., and L. Gomes (2001), Modeling mineral aerosol production by wind erosion: Emission intensities and aerosol distributions in source areas, *J. Geophys. Res*, *106*, 18,075–18,084.

Alfaro, S. C., A. Gaudichet, L. Gomes, and M. Maillé (1997), Modeling the size distribution of a soil aerosol produced by sandblasting, *J. Geophys. Res.*, *102*(D10), 11,239–11,249.

Alfaro, S. C., A. Gaudichet, L. Gomes, and M. Maillé (1998), Mineral aerosol production by wind erosion: Aerosol particle sizes and binding energies, *Geophys. Res. Lett.*, *25*(7), 991–994.

Alfaro, S. C., J. L. Rajot, and W. Nickling (2004), Estimation of PM20 emissions by wind erosion: Main sources of uncertainties, *Geomorphology, 59*, 63–74.

Andreae, M. O. (1995), Climate effects of changing atmospheric aerosol levels, in *World Survey of Climatology, Vol. 16, Future Climate of the World*, edited by A. Henderson-Sellers, pp. 341–392, Elsevier, Amsterdam.

Bagnold, R. A. (1941), *The Physics of Blown Sand and Desert Dunes*, 265 pp., Methuen, London.

Bauer, S. E., Y. Balkanski, M. Schulz, D. A. Hauglustaine, and F. Dentener (2004), Global modeling of heterogeneous chemistry on mineral aerosol surfaces: 1. The influence on tropospheric ozone chemistry and comparison to observations, *J. Geophys. Res.*, *109*, D02304, doi:10.1029/2003JD003868.

Bergametti, G., A. L. Dutot, P. Buat-Ménard, R. Losno, and E. Remoudaki (1989a), Seasonal variability of the elemental composition of atmospheric aerosol particles over the northwestern Mediterranean, *Tellus B.*, *41B*, 353–361.

Bergametti, G., L. Gomes, E. Remoudaki, M. Desbois, D. Martin, and P. Buat-Ménard (1989b), Present transport and deposition patterns of African dusts to the northwestern Mediterranean, in *Paleoclimatology and Paleometeorolgy: Modern and Past Patterns of Global Atmospheric Transport*, edited by M. Leinen and M. Sarnthein, pp. 227–251, Springer, Norwell, Mass.

Bergametti, G., E. Remoudaki, R. Losno, E. Steiner, B. Chatenet, and P. Buat-Ménard (1992), Sources, transport and deposition of atmospheric phosphorus over the northwestern Mediterranean, *J. Atmos. Chem.*, *14*, 501–513.

Betts, A. K., and A. C. M. Beljaars (2003), ECMWF ISLSCP-II near-surface dataset from ERA-40, *ERA-40 Proj. Rep. Ser.* from ECMWF, *8*, 31 pp., European Centre for Medium-Range Weather Forecasts, Reading, U.K.

Bouet, C., G. Cautenet, R. Washington, M. C. Todd, B. Laurent, B. Marticorena, and G. Bergametti (2007), Mesoscale modeling of aeolian dust emission during the BoDEx 2005 experiment, *Geophys. Res. Lett.*, *34*, L07812, doi:10.1029/2006GL029184.

Brooks, N. P. J., and M. Legrand (2000), Dust variability over northern Africa and rainfall in the Sahel, in *Linking Climate Change to Landsurface Change*, chap. 1, edited by S. J. McLaren and D. Kniveton, pp. 1–25, Springer, New York.

Cakmur, R. V., R. L. Miller, J. Perlwitz, I. V. Geogdzhayev, P. Ginoux, D. Koch, K. E. Kohfeld, I. Tegen, and C. S. Zender (2006), Constraining the magnitude of the global dust cycle by minimizing the difference between a model and observations, *J. Geophys. Res.*, *111*, D06207, doi:10.1029/2005JD005791.

Callot, Y., B. Marticorena, and G. Bergametti (2000), Geomorphologic approach for modeling the surface features of arid environments in a model of dust emissions: Application to the Sahara desert, *Geodin. Acta*, *13*, 245–270.

Chappell, A., A. Warren, A. O'Donoghue, A. Robinson, A. D. Thomas, and C. S. Bristow (2008), The implications for dust emission modeling of spatial and vertical variations in horizontal dust flux and particle size in the Bodélé Depression, northern Chad, *J. Geophys. Res.*, *113*, D04214, doi:10.1029/2007JD009032.

Chatenet, B., B. Marticorena, L. Gomes, and G. Bergametti (1996), Assessing the microped size distributions of desert soils erodible by wind, *Sedimentology*, *43*, 901–911.

Chepil, W. S. (1951), Properties of soil which influence wind erosion. part IV: State or dry aggregate structure, *Soil Sci.*, *72*, 387–401.

Chiapello, I. (1996), Les aérosols atmosphériques au dessus de l'Atlantique nord tropical: Approche physico-chimique et météorologique. Evaluation de la contribution de différentes espèces à l'épaisseur optique en aérosol, Thèse de doctorat, 251 pp., Université Paris 7, Paris, France.

D'Almeida, G. A. (1986), A model for Saharan dust transport, *J. Appl. Meteorol.*, *25*, 903–916.

Dayan, U. (1986), Climatology of back-trajectories from Israel based on synoptic analysis, *J. Appl. Meteorol.*, *25*, 591–603.

Dayan, U., J. L. Heffter, J. M. Miller, and G. Gutman (1991), Dust intrusion events into the Mediterranean basin, *J. Appl. Meteorol.*, *30*, 1185–1199.

Ding, Z. L., J. Z. Ren, S. L. Yang, and T. S. Liu (1999), Climate instability during the penultimate glaciation: Evidence from two high-resolution loess records, China, *J. Geophys. Res.*, *104*, 20,123–20,132.

Dubief, J. (1953), Les vents de sable dans le Sahara Français, *Colloques Internationaux du CNRS*, *35*, 45–70, Centre National de la Recherche Scientifique, Alger, Algeria.

Dubief, J. (1963), *Le Climat du Sahara, Tome 2, Mémoires de l'Institut de Recherches Sahariennes*, 275 pp., Université d'Alger, Alger, Algeria.

Duce, R. A. (1995), Sources, distributions, and fluxes of mineral aerosols and their relationship to climate, in *Aerosol Forcing of Climate*, edited by R. J. Charlson and J. Heintzenberg, pp. 43–72, John Wiley, New York.

Dumay, F., M. Mainguet, J. C. Georges, O. Fall, H. Guang, O. H. Lémine, and S. A. Lehbib (2002), End of the global wind action system Saharo-Sahelian in Western Africa, 12th ISCO Conference Beijing 2002, 223–231, Tsinghua University press, Beijing, China.

Engelstaedter, S., and R. Washington (2007), Atmospheric controls on the annual cycle of north African dust, *J. Geophys. Res.*, *112*, D03103, doi:10.1029/2006JD007195.

Engelstaedter, S., R. Washington, and I. Tegen (2006), North African dust emissions and transport, *Earth Sci. Rev.*, *79*, 73–100.

Fécan, F., B. Marticorena, and G. Bergametti (1999), Parameterization of the increase of the aeolian erosion threshold wind friction velocity due to soil moisture for semi arid areas, *Ann. Geophys.*, *17*, 149–157.

Gillette, D. A. (1974), On the production of soil wind erosion aerosols having the potential for long range transport, *J. Atmos. Res.*, *8*, 735–744.

Gillette, D. A. (1979), Environmental factors affecting dust emission by wind erosion, in *Saharan Dust*, edited by C. Morales, pp. 71–94, John Wiley, New York.

Gillette, D. A. (1981), Production of dust that may be carried great distances: Origin, characteristics and effect on man, *Spec. Pap. Geol. Soc. Am.*, *186*, 11–26.

Gillette, D. A., and P. H. Stockton (1989), The effect of nonerodible particles on wind erosion of erodible surfaces, *J. Geophys. Res.*, *94*, 12,885–12,893.

Gomes, L., G. Bergametti, G. Coudé-Gaussen, and P. Rognon (1990), Submicron desert dust: 1. A sandblasting process, *J. Geophys. Res.*, *95*, 13,927–13,935.

Gomes, L., J.-L. Rajot, S. C. Alfaro, and A. Gaudichet (2003), Validation of a dust production model from measurements performed in semi-arid agricultural areas of Spain and Niger, *Catena*, *52*, 257–271.

Goudie, A. S., and N. J. Middleton (2001), Saharan dust storms: Nature and consequences, *Earth Sci. Rev.*, *56*, 179–204.

Greeley, R., D. G. Blumberg, and S. H. Williams (1996), Field measurements of the flux and speed of wind-blown sand, *Sedimentology*, *43*, 41–52.

Greeley, R., D. G. Blumberg, J. F. McHone, A. Dobrovolski, J. Iversen, N. Lancaster, K. R. Rasmussen, S. Wall, and B. White (1997), Applications of spaceborne radar laboratory data to the study of aeolian processes, *J. Geophys. Res.*, *102*, 10,971–10,983.

Herman, J. R., P. K. Bhartia, O. Torres, C. Hsu, C. Seftor, and E. Celarier (1997), Global distribution of UV-absorbing aerosols from Nimbus 7/TOMS data, *J. Geophys. Res.*, *102*, 16,911–16,922.

Iversen, J. D., and B. R. White (1982), Saltation threshold on Earth, Mars and Venus, *Sedimentology*, *29*, 111–119.

Jickells, T. D., et al. (2005), Global iron connections: Between desert dust, ocean biogeochemistry and climate, *Science*, *308*, 67–71, 5708.

Kalu, A. E. (1979), The African dust plume: Its characteristics and propagation across West African winter, in *Saharan Dust*, edited by C. Morales, pp. 95–118, John Wiley, New York.

Kaufman, Y. J., I. Koren, L. A. Remer, D. Tanré, P. Ginoux, and S. Fan (2005), Dust transport and deposition observed from the Terra-Moderate Resolution Imaging Spectroradiometer (MODIS) spacecraft over the Atlantic Ocean, *J. Geophys. Res.*, *110*, D10S12, doi:10.1029/2003JD004436.

Koren, I., Y. J. Kaufman, R. Washington, M. C. Todd, Y. Rudich, J. V. Martins, and D. Rosenfeld (2006), The Bodélé depression: A single spot in the Sahara that provides most of the mineral dust to the Amazon forest, *Environ. Res. Lett.*, *1*, 014005, doi:10.1088/1748-9326/1/1/014005.

Kubilay, N., and A. C. Saydam (1995), Trace elements in atmospheric particulates over the eastern Mediterranean: Concentrations, sources, and temporal variability, *Atmos. Environ.*, *29*, 2289–2300.

Lafon, S. (2004), Les oxydes de fer dans l'aérosol désertique en relation avec ses propriétés optiques: Caractérisation physico-chimique de poussières minérales générées en soufflerie, Thèse de doctorat, 309 pp., Université Paris 12 Val-de-Marne, Créteil, France.

Laurent, B., B. Marticorena, G. Bergametti, P. Chazette, F. Maignan, and C. Schmechtig (2005), Simulation of the mineral dust emission frequencies from desert areas of China and Mongolia using an aerodynamic roughness length map derived from the POLDER/ADEOS 1 surface products, *J. Geophys. Res.*, *110*, D18S04, doi:10.1029/2004JD005013.

Laurent, B., B. Marticorena, G. Bergametti, and F. Mei (2006), Modeling mineral dust emissions from Chinese and Mongolian deserts, *Global Planet. Change*, *52*(1–4), 121–141.

Legrand, M., C. N'Doumé, and I. Jankowiak (1994), Satellite-derived climatology of the Saharan aerosol, in *Passive Infrared Remote Sensing of Clouds and the Atmosphere II: Proc. SPIE 2309*, edited by D. K. Lynch, pp. 127–135, Society of Photo-Optical Instrumentation Engineers, Bellingham, Wash.

Legrand, M., A. Plana-Fattori, and C. N'Doumé (2001), Satellite detection of dust using the IR imagery of Meteosat: 1. Infrared difference dust index, *J. Geophys. Res.*, *106*, 18,251–18,274.

Léon, J. F., and M. Legrand (2003), Mineral dust sources in the surroudings of the north Indian Ocean, *Geophys. Res. Lett.*, *30*(6), 1309, doi:10.1029/2002GL016690.

Leys, J. F., and M. R. Raupach (1991), Soil flux measurements with a portable wind erosion tunnel, *Aust. J. Soil Res.*, *29*, 533–552.

Lopez, M. V. (1998), Wind erosion in agricultural soil: An example of limited supply of particles available for erosion, *Catena*, *33*, 17–28.

Losno, R., G. Bergametti, P. Carlier, and G. Mouvier (1991), Major ions in marine rainwater with attention to sources of alkaline and acidic species, *Atmos. Environ.*, *25*, 771–777.

Loÿe-Pilot, M. D., J. M. Martin, and J. Morelli (1986), Influence of Saharan dust on the rain acidity and atmospheric input to the Mediterranean, *Nature*, *321*, 427–428.

Lu, H., and Y. Shao (1999), A new model for dust emission by saltation bombardment, *J. Geophys. Res.*, *104*, 16,827–16,842.

McKenna-Neuman, C., and W. G. Nickling (1989), A theoritical and wind tunnel investigation of the effect of capillarity water on the entrainment of sediment by wind, *Can. J. Soil Sci.*, *69*, 79–96.

Mainguet, M., and M. C. Chemin (1985), The concept of a sandy-aeolian sediment budget applied to the sand deposits of the Sahara and Sahel taken as a unit in the analysis of the surface shape types of the "Grand Ergs oriental et occidental", in *Proceedings of the International Workshop on "Sand Transport and Desertification in Arid Lands"*, November, Khartoum, Sudan, edited by F. El-Baz, I. A. El-Tayeb, and M. H. A. Hassan, World Sci., Singapore.

Mahowald, N., and C. Luo (2003), A less dusty future?, *Geophys. Res. Lett.*, *30*(17), 1903, doi:10.1029/2003GL017880.

Mahowald, N., K. Kohfeld, M. Hansson, Y. Balkanski, S. Harrison, C. Prentice, M. Schulz, and H. Rodhe (1999), Dust sources and deposition during the last glacial maximum and current climate: A comparison of model results with paleodata from ice cores and marine sediments, *J. Geophys. Res.*, *104*, 15,895–15,916.

Mahowald, N. M., J. A. Ballantine, J. Feddema, and N. Ramankutty (2007), Global trends in visibility: Implications for dust sources, *Atmos. Chem. Phys.*, *7*, 3309–3339.

Marticorena, B., and G. Bergametti (1995), Modeling the atmospheric dust cycle: 1. Design of a soil derived dust production scheme, *J. Geophys. Res.*, *100*, 16,415–16,430.

Marticorena, B., and G. Bergametti (1996), Two-years simulations of seasonal and interannual changes of the Saharan dust emissions, *Geophys. Res. Lett.*, *23*, 1921–1924.

Marticorena, B., G. Bergametti, B. Aumont, Y. Callot, C. N'Doumé, and M. Legrand (1997a), Modeling the atmospheric dust cycle: 2. Simulations of Saharan dust sources, *J. Geophys. Res.*, *102*, 4387–4404.

Marticorena, B., G. Bergametti, D. A. Gillette, and J. Belnap (1997b), Factors controlling threshold friction velocity in semiarid and arid areas of the United States, *J. Geophys. Res.*, *102*, 23,277–23,287.

Marticorena, B., P. Chazette, G. Bergametti, F. Dulac, and M. Legrand (2004), Mapping the aerodynamic roughness length of desert surfaces from the POLDER/ADEOS bi-directional reflectance product, *Int. J. Remote Sens.*, *25*, 603–626, 3.

Mei, F., X. Zhang, H. Lu, Z. Shen, and Y. Wang (2004), Characterization of MASDs of surface soils in north China and its influence on estimating dust emission, *Chin. Sci. Bull.*, *49*, 2169–2176, 20.

Middleton, N. J. (1986), A geography of dust storms in south-west Asia, *J. Climatol.*, *6*, 183–196.

Middleton, N. J., and A. S. Goudie (2001), Saharan dust: Sources and trajectories, *Trans. Inst. Br. Geogr.*, *26*, 165–181.

Mougin, E., D. Lo Seen, S. Rambal, A. Gaston, and P. Hiernaux (1995), A regional sahelian grassland model to be coupled with multispectral satellite data. part I: Model description and validation, *Remote Sens. Environ.*, *52*, 191–193.

Moulin, C., et al. (1998), Satellite climatology of African dust transport in the Mediterranean atmosphere, *J. Geophys. Res.*, *103*, 13,137–13,144.

Nickling, W. G. and J. A. Gillies (1989), Emission of fine-grained particulates from desert soils, in *Paleoclimatology and Paleometeorology: Modern and Past Patterns of Global Atmospheric Transport*, edited by M. Leinen and M. Sarnthein, pp. 133–165 Springer, Dordrecht.

Nickling, W. G., and S. A. Wolfe (1994), The morphology and origin of Nabhkas, region of Mopti, Mali, West Africa, *J. Arid Environ.*, *28*, 13–30.

Prospero, J. M., P. Ginoux, O. Torres, S. E. Nicholson, and T. E. Gill (2002), Environmental characterization of global sources of atmospheric soil dust identified with the Nimbus 7 Total Ozone Mapping Spectrometer (TOMS) absorbing aerosol product, *Rev. Geophys.*, *40*(1), 1002, doi:10.1029/2000RG000095.

Shao, Y. (2001), A model for mineral dust emission, *J. Geophys. Res.*, *106*, 20,239–20,254.

Shao, Y. (2004), Simplification of a dust emission scheme and comparison with data, *J. Geophys. Res.*, *109*, D10202, doi:10.1029/2003JD004372.

Shao, Y., M. R. Raupach, and P. A. Findlater (1993), Effect of saltation bombardment on the entrainment of dust by wind, *J. Geophys. Res.*, *98*, 12,719–12,726.

Sokolik, I. N., and O. B. Toon (1999), Incorporation of the mineralogical composition into models of the radiative properties of mineral aerosol from UV to IR wavelengths, *J. Geophys. Res.*, *104*(D8), 9423–9444.

Sörensen, M. (1985), Estimation of some aeolian saltation transport parameters from transport rate profiles, in *Proceedings of the International Workshop on the Physics of Blown Sand*, edited by O. E. Barndorff-Nielsen et al., pp. 141–190, Univ. of Aarhus, Aarhus, Denmark.

Swap, R., M. Garstang, S. Greco, R. Talbot, and J. Y. Gac (1992), Sahara dust in the Amazon basin, *Tellus, Ser. B*, *44*, 133–149.

Tegen, I., and I. Fung (1994), Modeling of mineral dust in the atmosphere: Sources, transport, and optical thickness, *J. Geophys. Res.*, *99*(D11), 22,897–22,914.

Tegen, I., M. Werner, S. P. Harrison, and K. E. Kohfeld (2004), Relative importance of climate and land use in determining present and future global soil dust emission, *Geophys. Res. Lett.*, *31*, L05105, doi:10.1029/2003GL019216.

Torres, O., P. K. Bhartia, J. R. Herman, Z. Ahmad, and J. Gleason (1998), Derivation of aerosol properties from satellite measurements of backscattered ultraviolet radiation: Theoretical basis, *J. Geophys. Res.*, *103*, 17,099–17,110.

Uppala, S., P. Kållberg, A. Hernandez, S. Saarinen, M. Fiorino, X. Li, K. Onogi, N. Sokka, U. Andrae, and V. Da Costa-Bechtold (2004), ERA-40: ECMWF 45-year reanalysis of the global atmosphere and surface conditions 1957–2002, ECMWF Newsletter no. 101, edited by Peter White, Shinfield Park, Reading, Berkshire RG2 9AX, U.K.

Valentin, C. (1991), Surface crusting in two alluvial soils of northern Niger, *Geoderma*, *48*, 201–222.

Valentin, C., J. L. Rajot, and D. Mitja (2004), Responses of soil crusting, runoff and erosion to fallowing in the sub-humid and semi-arid regions of West Africa, *Agric. Ecosyst. Environ.*, *104*, 287–302.

Warren, A., A. Chappell, M. C. Todd, C. Bristow, N. Drake, S. Engelstaedter, V. Martins, S. M'bainayel, and R. Washington (2007), Dust-raising in the dustiest place on Earth, *Geomorphology*, *92*(1–2), 25–37.

Washington, R., and M. C. Todd (2005), Atmospheric controls on mineral dust emission from the Bode'le' Depression, Chad: The role of the low level jet, *Geophys. Res. Lett.*, *32*, L17701, doi:10.1029/2005GL023597.

Washington, R., M. Todd, N. J. Middleton, and A. S. Goudie (2003), Dust-storm source areas determined by the Total Ozone Monitoring Spectrometer and surface observations, *Ann. Assoc. Am. Geogr.*, *93*(2), 297–313.

Webb, R. W., C. E. Rosenzweig, and E. R. Levine (2000), Global soil texture and derived water-holding capacities, Oak Ridge National Laboratory Distributed Active Archive Center, Oak Ridge, Tenn., doi:10.3334/ORNLDAAC/548.

White, B. R. (1979), Soil transport by winds on Mars, *J. Geophys. Res.*, *84*, 4643–4651.

Williams, G. (1964), Some aspects of the aeolian saltation load, *Sedimentology*, *3*, 253–256.

Yoshioka, M., N. Mahowald, J. L. Dufresne, and C. Luo (2005), Simulation of absorbing aerosol indices for African dust, *J. Geophys. Res.*, *110*, D18S17, doi:10.1029/2004JD005276.

Zender, C. S., R. Miller, and I. Tegen (2004), Quantifying mineral dust mass budgets: Terminology, constraints, and current estimates, *Eos Trans AGU*, *85*(48), 509–512.

Zobler, L. (1986), A world soil file for global climate modeling, NASA Technical Memorandum, 87802, NASA Goddard Institute for Space Studies, New York, N.Y.

G. Bergametti and B. Marticorena, Laboratoire Interuniversitaire des Systèmes Atmosphériques, 61 Avenue du Général de Gaulle, Universités Paris VII-XII, 94010, Créteil, France.

B. Laurent, Leibniz-Institut für Troposphärenforschung, Permoserstraße 15, 04318, Leipzig, Germany. (laurent@tropos.de)

J. F. Léon, Laboratoire d'Optique Atmosphérique, Université de Lille Bat P5 Cite scientifique, UMR CNRS 8518, 59655, Villeneuve-d'Ascq, France.

N. M. Mahowald, Department of Earth and Atmospheric Sciences, Cornell University, 2140 Snee Hall, Ithaca, NY 14853, USA.